

A Brief Note is a short paper that presents a specific solution of technical interest in mechanics but which does not necessarily contain new general methods or results. A Brief Note should not exceed 1500 words or equivalent (a typical one-column figure or table is equivalent to 250 words; a one line equation to 30 words). Brief Notes will be subject to the usual review procedures prior to publication. After approval such Notes will be published as soon as possible. The Notes should be submitted to the Editor of the JOURNAL OF APPLIED MECHANICS. Discussions on the Brief Notes should be addressed to the Editorial Department, ASME International, Three Park Avenue, New York, NY 10016-5990, or to the Editor of the JOURNAL OF APPLIED MECHANICS. Discussions on Brief Notes appearing in this issue will be accepted until two months after publication. Readers who need more time to prepare a Discussion should request an extension of the deadline from the Editorial Department.

## A New Lagrangian and a New Lagrange Equation of Motion for Fractionally Damped Systems

O. P. Agrawal

Professor, Mechanical Engineering and Energy Processes,  
Southern Illinois University, Carbondale, IL 62901

### 1 Introduction

All dynamic systems exhibit some degree of internal damping. Recent investigations have shown that a fractional derivative model provides a better representation of the internal damping of a material than an ordinary derivative model does. For a survey of fractional damping models and their applications to engineering systems, the readers are referred to Rossikhin and Shitikova [1] and the references therein. Traditionally, the Newton's law is used to model such nonconservative systems, and when a Lagrangian, Hamiltonian, variational, or other energy-based approach is used, it is modified so that the resulting equations match those obtained using the Newtonian's approach.

Several attempts have been made to include nonconservative forces in the Lagrangian and the Hamiltonian mechanics. Riewe [2,3] presented a succinct survey of research in this area. He also pointed out that a term proportional to  $d^n x/dt^n$  in the Euler-Lagrange equation follows from a Lagrangian with a term proportional to  $(d^{n/2}x/dt^{n/2})^2$ . Hence, a frictional force of the form  $c(dx/dt)$  may follow directly from a Lagrangian containing a term of the form  $(d^{1/2}x/dt^{1/2})^2$ . Using this as the starting point, he developed a new approach to mechanics that allows nonconservative terms (both ordinary and fractional damping) to be included in Lagrangians and Hamiltonians. This paper presents another form of a Lagrangian and the Lagrange equation that can be used to obtain equations of motion of systems whose damping forces are proportional to a fractional derivative of order  $j/n$ . With a minor change in the formulation, the resulting equations can be thought of as a state space representation of Riewe's formulation ([2,3]).

Contributed by the Applied Mechanics Division of THE AMERICAN SOCIETY OF MECHANICAL ENGINEERS for publication in the ASME JOURNAL OF APPLIED MECHANICS. Manuscript received by the ASME Applied Mechanics Division, June 7, 1999; final revision, Apr. 24, 2000. Associate Editor: A. A. Ferri.

### 2 A New Lagrangian and a New Lagrange Equation of Motion

This section presents a new Lagrangian and a new Lagrange equation of motion for a fractionally damped system. There are several definitions of a fractional derivative. Here a fractional derivative is defined in the Riemann-Liouville sense ([4]):

$$D^\alpha x(t) = \frac{d^\alpha x(t)}{dt^\alpha} = \frac{1}{\Gamma(1-\alpha)} \frac{d}{dt} \int_0^t \frac{x(t-u)}{u^\alpha} du, \quad t > 0, \quad 0 < \alpha < 1. \quad (1)$$

This definition can be extended for  $\alpha > 1$ . Here  $x(t)$  represents a state space coordinate of the dynamical system. The Lagrangian and the Lagrange equation of motion are given as

$$L = \nu_1(\alpha) \frac{1}{2} (D^\alpha y)^T M D^\alpha y - \frac{1}{2} y^T K y + Q^T y, \quad (2)$$

and

$$\nu_1^{-1}(\alpha) \frac{d^\alpha}{dt^\alpha} \frac{\partial L}{\partial (D^\alpha y)} - \frac{\partial L}{\partial y} = 0 \quad (3)$$

where  $y$  is a state vector,  $M$  and  $K$  are the mass-like and the stiffness-like matrices,  $\nu_1(\alpha)$  is a  $\alpha$ -dependent coefficient, and  $Q$  is a vector of generalized forces. The purpose of  $\nu_1(\alpha)$  is to make the formulation consistent with the variational (or Euler-Lagrange) approach ([2,3]). Since  $\nu_1(\alpha)$  does not appear in the equations of motion, it will not be included, and its expression will not be given here (for its expression see [2,3]). The Lagrangian  $L$  defined in Eq. (2) is applicable for positive rational  $\alpha$  only. The dimensions of  $y$ ,  $M$ , and  $K$  depend on the denominator part of  $\alpha$ . Therefore, in this setting,  $L$  cannot be developed for irrational  $\alpha$ . Matrices  $M$  and  $K$  are not the traditional mass and stiffness matrices. It will be seen that  $M$  may contain the mass and the damping, and  $K$  may contain the mass, the damping, and the stiffness. In the case of zero damping,  $M$  and  $K$  reduce to the mass and the stiffness matrices. It is assumed that, for the functions considered here, the composition rule applies.

Substituting Eq. (2) into Eq. (3), we get the equation of motion as

$$M D^{2\alpha} y + K y = Q. \quad (4)$$

To generate  $L$ , we need  $\alpha$ ,  $y$ ,  $M$ ,  $K$ , and  $Q$ .  $\alpha$  is half of the lowest common fractional derivative order. Thus, for a force of the form  $(d^{j/n}x/dt^{j/n})$ ,  $\alpha = 1/(2n)$ .  $\alpha$  can be smaller. However, the smaller  $\alpha$  introduces no new modeling capability. The elements of the

state vector  $y$  are defined as  $y_i = D^{2\alpha}y_{i+1} = D^{1/n}y_{i+1}$ , ( $i = 1, \dots, l-1$ ), and  $y_l = x(t)$ , where  $l=2n$  is the dimension of the vector.

Now consider that  $mD^{2\alpha}x$ ,  $cD^{j/n}x$ , and  $kx$  represent the inertia, the damping, and the spring forces, where  $m$ ,  $c$ , and  $k$  are, respectively, the mass, the damping coefficient, and the stiffness of the system. In this case,  $M$  and  $K$  are given as

$$M = \begin{bmatrix} 0 & \cdots & 0 & \cdots & m \\ \vdots & \cdots & \vdots & \ddots & \vdots \\ 0 & \cdots & m & \cdots & c \\ \vdots & \ddots & \vdots & \ddots & \vdots \\ m & \cdots & c & \cdots & 0 \end{bmatrix},$$

$$K = \begin{bmatrix} 0 & \cdots & \cdots & 0 & -m & 0 \\ \vdots & \ddots & \ddots & \ddots & \ddots & 0 \\ \vdots & \ddots & \ddots & \ddots & -c & 0 \\ 0 & \ddots & \ddots & \ddots & \ddots & \vdots \\ -m & \ddots & -c & 0 & \ddots & 0 \\ 0 & 0 & 0 & \cdots & 0 & k \end{bmatrix}. \quad (5)$$

In matrix  $M$  the off-diagonal contains  $m$  and the  $j$ th off-diagonal measured from the bottom right corner contains  $c$ . In matrix  $K$  the bottom right corner contains  $k$ , the elements left to the off-diagonal contain  $-m$ , and all except the first and the last elements of the  $(j+1)$ th off-diagonal measured from the bottom right corner contains  $-c$ . Note that  $M$  and  $K$  are symmetric. Structure of these matrices will be explained further using two examples. Finally, vector  $Q$  is given as

$$Q = [0, \dots, 0, F] \quad (6)$$

where  $F$  is the generalized force.

The Lagrangians and the Lagrange equations of motion for two fractionally damped systems are given below.

*Example 1.* Damping force =  $c\dot{x}$ .

For this system,  $\alpha=1/2$ . Vector  $y$ , matrices  $M=M_1$  and  $K=K_1$ , the Lagrangian  $L$ , and the Lagrange equation are

$$y = [y_1 \ y_2]^T = [\dot{x} \ x]^T,$$

$$M_1 = \begin{bmatrix} 0 & m \\ m & c \end{bmatrix}, \quad K_1 = \begin{bmatrix} -m & 0 \\ 0 & k \end{bmatrix},$$

$$L = \frac{1}{2}(D^{1/2}y)^T M_1 D^{1/2}y - \frac{1}{2}y^T K_1 y,$$

$$\frac{d^{1/2}}{dt^{1/2}} \frac{\partial L}{\partial(D^{1/2}y)} - \frac{\partial L}{\partial y} = 0.$$

These terms give  $M_1 D y + K_1 y = 0$ , which is equivalent to  $m\ddot{x} + c\dot{x} + kx = 0$ .

*Example 2.* Damping force =  $cD^{4/3}x$ .

This example shows the locations of  $c$  when  $j$  in the force term  $cD^{j/n}x$  is more than 1. For this system,  $\alpha=1/6$ . Vector  $y$ , matrices  $M=M_2$  and  $K=K_2$ , the Lagrangian  $L$ , and the Lagrange equation are

$$y = [y_1 \ y_2 \ y_3 \ y_4 \ y_5 \ y_6]^T$$

$$= [D^{5/3}x \ D^{4/3}x \ D^{1/3}x \ D^{2/3}x \ D^{1/3}x \ x]^T,$$

$$M_2 = \begin{bmatrix} 0 & 0 & 0 & 0 & 0 & m \\ 0 & 0 & 0 & 0 & m & 0 \\ 0 & 0 & 0 & m & 0 & c \\ 0 & 0 & m & 0 & c & 0 \\ 0 & m & 0 & c & 0 & 0 \\ m & 0 & c & 0 & 0 & 0 \end{bmatrix},$$

$$K_2 = \begin{bmatrix} 0 & 0 & 0 & 0 & -m & 0 \\ 0 & 0 & 0 & -m & 0 & 0 \\ 0 & 0 & -m & 0 & -c & 0 \\ 0 & -m & 0 & -c & 0 & 0 \\ -m & 0 & -c & 0 & 0 & 0 \\ 0 & 0 & 0 & 0 & 0 & k \end{bmatrix},$$

$$L = \frac{1}{2} (D^{1/6}y)^T M_2 D^{1/6}y - \frac{1}{2} y^T K_2 y,$$

$$\frac{d^{1/6}}{dt^{1/6}} \frac{\partial L}{\partial(D^{1/6}y)} - \frac{\partial L}{\partial y} = 0.$$

These terms give  $M_2 D^{1/3}y + K_2 y = 0$ , which is equivalent to  $m\ddot{x} + cD^{4/3}x + kx = 0$ .

Note that  $M$  may contain  $m$  and  $c$ , and  $K$  may contain  $m$ ,  $c$ , and  $k$ . Also, note that in the examples  $c$  can be set to zero to obtain the differential equations of motion of an undamped system in a higher dimension. Similarly,  $\alpha$  in Example 1 can be set to 1/4 to obtain the differential equations of motion of a damped system in a higher dimension. However, such increase in dimensions adds no benefit. Further, as the order of the fractional derivative  $\alpha$  moves from 1 towards 0 (1 towards 2) the damper behaves like a spring (mass).

Several techniques have been developed to solve the resulting set of fractional differential equations. Suarez and Shokooh [5] presented an eigenvector expansion method to solve these differential equations. Other methods to solve these fractional differential equations include, for example, Laplace transform and direct techniques similar to the techniques for ordinary differential equations ([6–8]), and the numerical techniques ([9]).

### 3 Additional Remarks

Riewe [2,3] developed a new approach to mechanics with fractional derivatives that includes the nonconservative Hamiltonian, Canonical transformations and the Jacobi theory. The approach can also be used to develop similar Hamiltonians and the Hamilton equations. To this end, we propose the following Hamiltonian and Hamilton equations for fractional systems.

$$H = (D^\alpha y)^T p - L = (D^\alpha y)^T p - \frac{1}{2}(D^\alpha y)^T M D^\alpha y + \frac{1}{2}y^T K y,$$

$$\frac{\partial H}{\partial p} = D^\alpha y, \quad \text{and} \quad \frac{\partial H}{\partial y} = -D^\alpha p,$$

where  $p = M D^\alpha y$ . It can be shown that the above equations lead to the correct equation of motion. Using these equations, the Hamiltonian can also be written as

$$H = \frac{1}{2}(D^\alpha p)^T M^{-1} D^\alpha p + \frac{1}{2}y^T K y,$$

which is similar to the total energy term for a conservative system.

### Acknowledgment

The author would like to thank the reviewers for their suggestions to improve the quality of the paper.

### References

- [1] Rossikhin, Y. A., and Shitikova, M. V., 1997, "Applications of Fractional Calculus to Dynamic Problems of Linear and Nonlinear Hereditary Mechanics of Solids," *Appl. Mech. Rev.*, **50**, No. 1, pp. 15–67.
- [2] Riewe, F., 1996, "Nonconservative Lagrangian and Hamiltonian Mechanics," *Phys. Rev. E*, **53**, No. 2, pp. 1890–1899.
- [3] Riewe, F., 1997, "Mechanics With Fractional Derivative," *Phys. Rev. E*, **55**, No. 3, pp. 3581–3592.
- [4] Oldham, K. B., and Spanier, J., 1974, *The Fractional Calculus*, Academic Press, New York.
- [5] Suarez, L. E., and Shokooh, A., 1997, "An Eigenvector Expansion Method for the Solution of Motion Containing Fractional Derivatives," *ASME J. Appl. Mech.*, **64**, pp. 629–635.
- [6] Miller, K. S., and Ross, B., 1993, *An Introduction to the Fractional Calculus*

and *Fractional Differential Equations*, John Wiley and Sons, New York.

- [7] Mainardi, F., 1997, "Fractional Calculus: Some Basic Problems in Continuum and Statistical Mechanics," *Fractals and Fractional Calculus in Continuum Mechanics*, A. Carpinteri and F. Mainardi, eds., Springer-Verlag, New York, pp. 291–348.
- [8] Podlubny, I., 1999, *Fractional Differential Equations*, Academic Press, New York.
- [9] Yuan, L., and Agrawal, O. P., 1998, "A Numerical Scheme for Dynamical Systems Containing Fractional Derivatives," *Proceedings of the DETC98, ASME Design Engineering Technical Conferences*, Paper No. DETC98/MECH 5857, Sept. 13–16, Atlanta, GA.

## On the Unification of Yield Criteria

### S. C. Fan

Associate Professor, School of Civil & Structural Engineering, Nanyang Technological University, Nanyang Avenue, Singapore 639798

### M.-H. Yu

Professor, School of Civil Engineering & Mechanics, Xi'an Jiaotong University, Xi'an 710049, China

### S.-Y. Yang

Post Doctoral Fellow, School of Civil & Structural Engineering, Nanyang Technological University, Nanyang Avenue, Singapore 639798

*A piecewise linear unified yield criterion called the twin-shear-unified was proposed. It is based on a kind of orthogonal dodecahedron stress element. The effects of intermediate principal stress are taken into account such that most available yield loci on the  $\pi$ -plane are embraced in a unified manner. Besides, it is capable to represent not only convex limit surfaces but also nonconvex limit surfaces. [DOI: 10.1115/1.1320451]*

## 1 Introduction

For many engineering materials, two characteristic strength properties are crucial, i.e., initial and subsequent yield properties. The initial yield defines the critical state when the material under the complex stress state starts to yield. The subsequent yield deals with the post yield phenomena. It describes the material behavior beyond the initial yield. The initial yield provides the basis. As long as the initial yield property is defined, the remaining task is to define the different hardening/softening properties and to incorporate them into the initial yield provided. In this note, the yield criteria will be confined to the initial yield properties unless otherwise stated.

Generally speaking, yield criteria can be classified into two categories. The first category has originated from the concept of a single shear stress yield criterion such as the Tresca and the Mises. The Tresca is a maximum principal shear stress  $\tau_{\max}$  criterion. The Mises is an octahedral shear stress  $\tau_{\text{oct}}$  criterion. They both postulate that when  $\tau_{\max}$  (or  $\tau_{\text{oct}}$ ) reaches a critical value, the material begins to yield. Both the Tresca and the Mises are applicable only to materials with (i) equal tensile and compressive strengths  $\sigma_t = \sigma_c$ ; (ii) linear failure loci on the meridian plane (i.e., parallel to the hydrostatic axis which is represented by the

line  $\sigma_1 = \sigma_2 = \sigma_3$  in the principal stress space). Many derivatives of these two criteria have been proposed to model a wider range of engineering materials. Among them, the well-known ones are Mohr-Coulomb, Hoek-Brown, and Johnson (Tresca's derivatives), Matsuoka and Lade (Mises' derivatives) [1]. The Mohr-Coulomb is a  $\tau_{\max} - \sigma_\tau$  criterion which considers the effect of  $\tau_{\max}$  as well as the normal stress  $\sigma_\tau$  on the same plane. The introduction of  $\sigma_\tau$  makes it capable of simulating materials with different tensile and compressive strengths  $\sigma_t \neq \sigma_c$  (called the strength differential effect or SD effect). The Hoek-Brown and Johnson are Mohr-Coulomb's derivatives for rock. They take into account the effect of nonlinear failure loci on the meridian plane while the Mohr-Coulomb does not. The Matsuoka and Lade are failure theories for soil (sand). They account for both the SD effect and the nonlinear failure loci on the meridian plane.

Unfortunately, recent research revealed that those theories do not necessarily represent the real failure/yield of materials under complex stress state. One prominent feature has been ignored, i.e., the effect of the intermediate principal stress ( $\sigma_2$ ). The Tresca and its derivatives ignore this effect whereas the Mises and its derivatives average the effects of all the three principal stresses  $\sigma_1, \sigma_2, \sigma_3$ . Experiments show that the  $\sigma_2$  effect varies from case to case ([2–5]). The extent of the  $\sigma_2$  effect depends on the material type and the stress state.

The second category of yield criteria may be called curve-fitting multiparameter criteria such as the Argyris-Gudehus-Zienkiewicz criterion, the Willam-Warnke criterion, and some smooth models ([1]). These criteria usually have complex mathematical expressions because simple expressions usually cannot reflect the diversity of test results. The main advantage is that they can simulate accurately the yield properties in the particular range of complex stress state where most tests are conducted. Another deficiency is that they have little physical background.

## 2 Twin Shear Unified Strength Criterion (TS-Unified)

**2.1 The TS-Unified Criterion Bridges Most Available Theories on  $\pi$  Plane.** The TS-unified is an extension of the twin shear yield criterion (TS) ([6]) and the generalized twin shear yield criterion (GTS) ([7]). The TS is based on a kind of orthogonal dodecahedron (OD) stress element and it assumes that when a function of the two larger principal shear stresses ( $\tau_{13}, \tau_{12}$ ) or ( $\tau_{13}, \tau_{23}$ ) reaches a critical value, the material begins to yield, i.e.,

$$\begin{aligned} \tau_{13} + \tau_{12} &= \sigma_t & \text{when } \tau_{12} \geq \tau_{23} \\ \tau_{13} + \tau_{23} &= \sigma_t & \text{when } \tau_{12} \leq \tau_{23} \end{aligned} \quad (1)$$

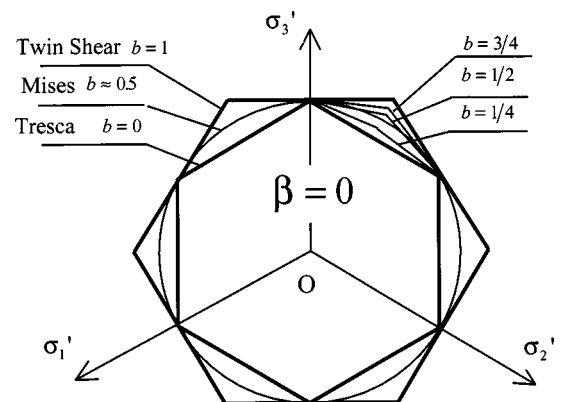


**Fig. 1 Different yield loci on the  $\pi$ -plane for non-SD materials ( $\sigma_t = \sigma_c$  or  $\beta = 0$ )**

Contributed by the Applied Mechanics Division of THE AMERICAN SOCIETY OF MECHANICAL ENGINEERS for publication in the ASME JOURNAL OF APPLIED MECHANICS. Manuscript received and accepted by the ASME Applied Mechanics Division, Feb. 16, 1999; final revision, Nov. 1, 2000. Associate Editor: M.-J. Pindera.

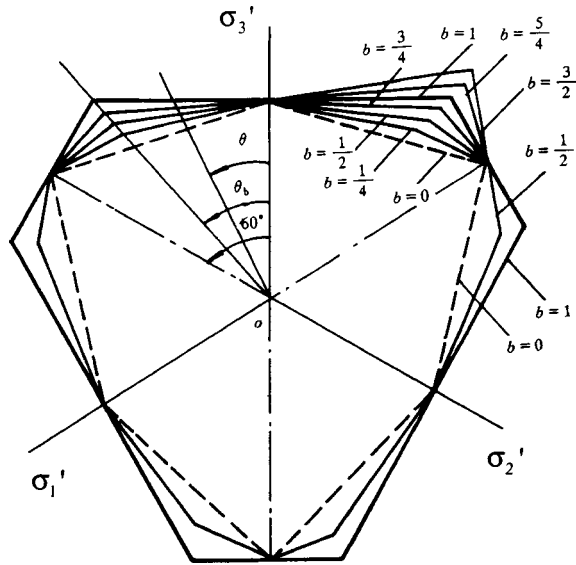


Fig. 2 Different yield loci on the  $\pi$ -plane for SD materials ( $\sigma_i \neq \sigma_c$  or  $\beta \neq 0$ )

where  $\tau_{13}=(\sigma_1-\sigma_3)/2$ ,  $\tau_{23}=(\sigma_2-\sigma_3)/2$ ,  $\tau_{12}=(\sigma_1-\sigma_2)/2$  are the principal shear stresses.  $\sigma_1$ ,  $\sigma_2$  and  $\sigma_3$  ( $\sigma_1 \geq \sigma_2 \geq \sigma_3$ ) are the principal normal stresses.  $\sigma_t$  is the uniaxial tensile strength.

The TS is an upper limit surface in the stress space complying with Drucker's convexity postulate and is used for non-SD materials ( $\sigma_t = \sigma_c$ , where  $\sigma_c$  is the uniaxial compressive strength) only. It is the counterpart to the Tresca, as shown in Fig. 1. The GTS extends the idea and assumes that the yield surface is a function of two larger principal shear stresses ( $\tau_{13}, \tau_{12}$ ) or ( $\tau_{13}, \tau_{23}$ ) and their corresponding normal stresses ( $\sigma_{13}, \sigma_{12}$ ) or ( $\sigma_{13}, \sigma_{23}$ ), i.e.,

$$\tau_{13} + \tau_{12} + \beta(\sigma_{13} + \sigma_{12}) = \frac{2\sigma_t\sigma_c}{\sigma_c + \sigma_t} \quad \text{when } \tau_{12} + \beta\sigma_{12} \geq \tau_{23} + \beta\sigma_{23} \quad (2)$$

$$\tau_{13} + \tau_{23} + \beta(\sigma_{13} + \sigma_{23}) = \frac{2\sigma_t\sigma_c}{\sigma_c + \sigma_t} \quad \text{when } \tau_{12} + \beta\sigma_{12} \leq \tau_{23} + \beta\sigma_{23}$$

where  $\sigma_{13}=(\sigma_1+\sigma_3)/2$ ,  $\sigma_{12}=(\sigma_1+\sigma_2)/2$ ,  $\sigma_{23}=(\sigma_2+\sigma_3)/2$ . The parameter  $\beta$  reflects the effects of the normal stresses so that SD effect can be represented. Likewise, the GTS serves as the counterpart to the Mohr-Coulomb, as shown in Fig. 2. When

$\beta=0$ , the GTS is simplified to the TS. So the TS is a special case of the GTS.

In the TS and GTS, the largest stresses (both the shear and the normal stresses) have the same extent of influence as that of the second largest. When different weight parameters are employed to reflect the different effects of the largest stresses and the second largest, the GTS can be generalized to the TS-unified. The TS-unified can be expressed as

$$\tau_{13} + b\tau_{12} + \beta(\sigma_{13} + b\sigma_{12}) = C \quad \text{when } \tau_{12} + \beta\sigma_{12} \geq \tau_{23} + \beta\sigma_{23} \quad (3)$$

$$\tau_{13} + b\tau_{23} + \beta(\sigma_{13} + b\sigma_{23}) = C \quad \text{when } \tau_{12} + \beta\sigma_{12} \leq \tau_{23} + \beta\sigma_{23}$$

where  $b$  is a material parameter which represents the effect of the intermediate (the second largest) principal stresses. The value of  $b$  can be determined by material tests.  $\beta$  and  $C$  are also material parameters. If uniaxial tensile and compressive strength ( $\sigma_t$  and  $\sigma_c$ ) are chosen as the basic test points, then  $\beta$  and  $C$  can be expressed as

$$\beta = \frac{\sigma_c - \sigma_t}{\sigma_c + \sigma_t} = \frac{1 - \alpha}{1 + \alpha} \quad C = \frac{(1+b)\sigma_t\sigma_c}{\sigma_c + \sigma_t} = \frac{1+b}{1+\alpha}\sigma_t \quad (4)$$

where  $\alpha = \sigma_t/\sigma_c$  is the ratio of the tensile to the compressive strengths. The ratio is an index of the material strength differential effect (SD effect).

The TS-unified is a series of piecewise linear yield criteria on the  $\pi$ -plane as shown in Figs. 1 and 2. The exact form of expression depends on the choice of parameter  $b$ , which in turn can be determined by some basic test results as illustrated in Section 2.3 of this note. The TS-unified has the following characteristics as shown in Table 1:

(a) With different choices of parameter  $b$ , the TS-unified can be simplified to the Tresca ( $\beta=0$  and  $b=0$ ), the linear approximations of Mises ( $\beta=0$  and  $b=1/2$  or  $\beta=0$  and  $b=1/(1+\sqrt{3})$ ), the Mohr-Coulomb ( $\beta \neq 0$  and  $b=0$ ), the TS ( $\beta=0$  and  $b=1$ ), the GTS ( $\beta \neq 0$  and  $b=1$ ) and a series of new strength criteria (other values of parameters  $\beta$  and  $b$ ).

(b) In the stress space, the lower and upper bounds for the yield surfaces on the  $\pi$ -plane are special cases of the TS-unified, i.e.,  $b=0$  ( $\beta=0$  for the Tresca or  $\beta \neq 0$  for the Mohr-Coulomb) and  $b=1$  ( $\beta=0$  for the TS or  $\beta \neq 0$  for the GTS), respectively.

(c) When the parameter  $b$  varies between 0 and 1, a series of yield surfaces between the two limiting surfaces can be obtained.

(d) When the parameter  $b$  varies beyond the range (i.e.,  $b < 0$  or  $b > 1$ ), a series of nonconvex limit surfaces could be derived.

**2.2 The TS-Unified Reflects Different  $\sigma_2$  Effects.** The Lode angle  $\theta_\sigma$  is a parameter to represent the relative value of  $\sigma_2$

Table 1 The characteristics of TS-unified

	$\beta=0$ ( $\sigma_t = \sigma_c = \sigma_0$ )	$\beta \neq 0$ ( $\sigma_t \neq \sigma_c$ )	Drucker's Convex Postulate
$b=0$	Tresca	Mohr-Coulomb	Lower bound
$\pi$ plane loci	Regular hexagon	Irregular hexagon	
Restriction for application	$\tau_0 = \frac{\sigma_0}{2}$	$\tau_0 = \frac{\sigma_t\sigma_c}{\sigma_c + \sigma_t}$	
$0 < b < 1$	New theories	New theories	Intermediate
$\pi$ plane loci	Irregular dodecagon	Irregular dodecagon	
Restriction for applications	$\tau_0 = \frac{(b+1)}{(2+b)}\sigma_0$	$\tau_0 = \frac{(b+1)\sigma_t\sigma_c}{\sigma_t + (b+1)\sigma_c}$	
$b=1$	Twin shear theory	Twin shear theory	Upper bound
$\pi$ plane loci	Regular hexagon	Irregular hexagon	
Restriction for applications	$\tau_0 = \frac{2}{3}\sigma_0$	$\tau_0 = \frac{2\sigma_t\sigma_c}{\sigma_t + 2\sigma_c}$	

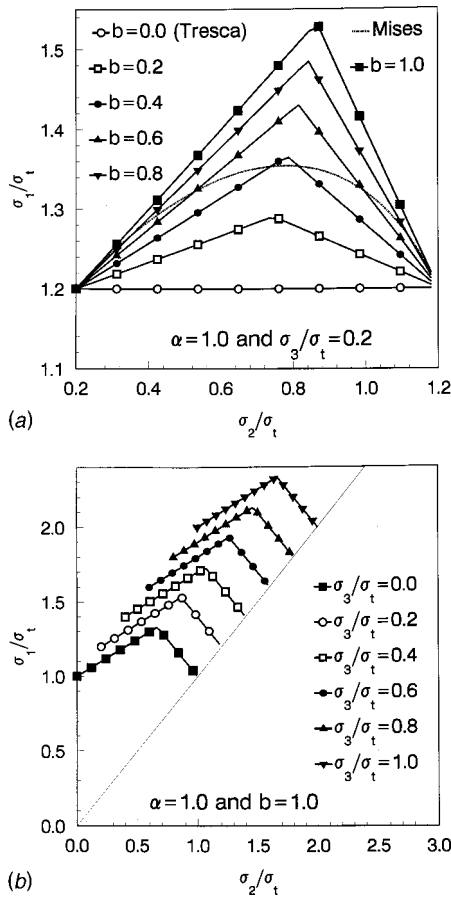


Fig. 3 TS-unified can reflect the  $\sigma_2$  effect in a piecewise linear manner; (a)  $\alpha=1$  and  $\sigma_3/\sigma_t=0.2$  case; (b)  $\alpha=1$  and  $b=1$  case

with respect to  $\sigma_1$  and  $\sigma_3$ . To reflect the  $\sigma_2$  effect, a theory should embed this parameter in its expression either in explicit or in implicit forms.

The TS-unified is usually expressed in terms of the stress (deviatoric) invariants, that is the first invariant of stress tensor  $I_1$ , the second invariant of stress deviatoric tensor  $J_2$ , and the stress angle  $\theta$ , as follows:

$$\frac{I_1}{3}(1-\alpha) + \left(1 + \frac{\alpha}{2}\right) \frac{2\sqrt{J_2}}{\sqrt{3}} \cos \theta - \frac{\alpha(1-b)}{1+b} \sqrt{J_2} \sin \theta = \sigma_t \quad \text{when } 0 \text{ deg} \leq \theta \leq \theta_b \quad (5)$$

$$\frac{I_1}{3}(1-\alpha) + \left(\frac{2-b}{1+b} + \alpha\right) \frac{\sqrt{J_2}}{\sqrt{3}} \cos \theta - \left(\alpha + \frac{b}{1+b}\right) \sqrt{J_2} \sin \theta = \sigma_t \quad \text{when } \theta_b \leq \theta \leq 60 \text{ deg}$$

where  $\theta_b$  is the stress angle when the two Eqs. (5) are equal:

$$\theta_b = \text{tg}^{-1} \frac{\sqrt{3}}{1+2\alpha}, \quad (0 \text{ deg} < \theta_b < 60 \text{ deg}). \quad (6)$$

The stress angle  $\theta$  is defined to reflect the  $\sigma_2$  effect as shown in Fig. 2, such that

$$\theta = \frac{1}{3} \cos^{-1} \frac{3\sqrt{3}}{2} \frac{J_3}{\sqrt{J_2^3}} \quad (0 \leq \theta \leq \pi/3). \quad (7)$$

It should be noted that the stress angle  $\theta$  is different from the Lode angle  $\theta_\sigma$ , and they are related as follows:

$$\theta = \frac{\pi}{6} - \theta_\sigma. \quad (8)$$

Equation (5) is the explicit expression for the TS-unified in terms of the stress angle  $\theta$ . With different choices of the parameter  $b$ , the TS-unified can reflect different piecewise linear  $\sigma_2$  effects. Two illustrations are given. Figure 3(a) shows the curves of  $\sigma_1/\sigma_t$  versus  $\sigma_2/\sigma_t$  for  $\alpha=1$  and  $\sigma_3/\sigma_t=0.2$ . Obvious strength difference can be observed when different criteria are adopted (represented by different values of the parameter  $b$ ). The maximum difference is about 25 percent. Figure 3(b) shows the curves for  $\alpha=1$  and  $b=1$ . The same conclusion can be drawn as from Fig. 3(a). In other words, the TS-unified is capable of representing variable strengths of the same material under different stress states.

**2.3 Application of the TS-Unified.** If  $\sigma_t$ ,  $\sigma_c$  and the shear strength  $\tau_0$  are chosen as the basic material parameters, through Eq. (3) for pure shear loading, the parameter  $b$  can be expressed as

$$b = \frac{(\sigma_c + \sigma_t)\tau_0 - \sigma_t\sigma_c}{(\sigma_t - \tau_0)\sigma_c}. \quad (9)$$

The parameter  $b$  plays an important role in the TS-unified. It builds a bridge among different strength theories. It is this parameter that distinguishes one theory from another. On the other hand, the scope of application of each theory is also represented by this parameter. Hence, the TS-unified is a unified theory that can be applied to more than one kind of material. In practice, when basic material parameters are obtained by experiments, the value of  $b$  can be determined through Eq. (9). Whenever parameter  $b$  is obtained, the yield criterion is determined and the application is possible ([8]).

### 3 Conclusions

A piecewise linear unified yield criterion called the TS-unified was proposed. Besides the capability that the TS-unified can bridge most available yield loci on the  $\pi$ -plane for both SD and non-SD materials, the most prominent characteristics of the criterion are their capability to represent the effects of the intermediate principal stress  $\sigma_2$  in piecewise linear forms. Illustrations were given. The determination of the parameters was also discussed.

Future research could focus on the pursuit for some criteria that can bridge different criteria both on the  $\pi$ -plane and on the meridian plane. It is obvious that the representation for nonlinear meridian loci can be obtained by adopting multiparameter criterion instead of the proposed two-parameter TS-unified.

### References

- [1] Chen, W. F., and Han, D. J., 1988, *Plasticity for Structural Engineers*, Springer-Verlag, New York.
- [2] Mogi, K., 1967, "Effect of Intermediate Principal Stress on Rock Failure," *J. Geophys. Res.*, **72**, pp. 5117-5131.
- [3] Michelis, P., 1987, "True Triaxial Cyclic Behavior of Concrete and Rock in Compression," *Int. J. Plast.*, **3**, No. 2, pp. 249-270.
- [4] Faruque, M. O., and Chang, C. J., 1990, "A Constitutive Model for Pressure Sensitive Materials With Particular Reference to Plain Concrete," *Int. J. Plast.*, **6**, No. 1, pp. 29-43.
- [5] Li, X. C., and Xu, D. J., 1990, "Experimental Verification of Twin Shear Strength Theory—The Strength Properties of Granite Under True Triaxial Stress State," Wuhan Institute of Rock and Soil Mechanics, Chinese Academy of Science, Paper Yantu (90) 52 (in Chinese).
- [6] Yu, M. H., 1983, "Twin Shear Stress Yield Criterion," *Int. J. Mech. Sci.*, **25**, No. 1, pp. 71-74.
- [7] Yu, M. H., He, L. N., and Song, L. Y., 1985, "Twin Shear Stress Theory and Its Generalization," *Sci. Sinica A*, **28**, No. 1, pp. 1174-1183.
- [8] Yu, M. H., Yang, S.-Y., and Fan, S. C., 1999, "Unified Elasto-Plastic Associated and Non-Associated Constitutive Model," *Comput. Struct.*, **71**, No. 6, pp. 627-636.

# Analytical Solution for W-N Criteria for the Prediction of Notched Strength of an Orthotropic Shell

**R. Ramesh Kumar**

Engineer, Structural Design and Analysis Division, Structural Engineering Group, Vikram Sarabhai Space Centre, Thiruvananthapuram 695 022, India

**S. Jose**

Senior Lecturer, Department of Mechanical Engineering, T.K.M. College of Engineering, Kollam 691 005, India

**G. Venkateswara Rao**

Group Director, Structural Design and Analysis Division, Structural Engineering Group, Vikram Sarabhai Space Centre, Thiruvananthapuram 695 022, India

*Analytical solution for the tangential stress distribution ahead of a hole is needed for the theoretical prediction of notched strength of brittle laminate using the well-known W-N criteria. In the present study, tangential stress distribution in an orthotropic circular cylindrical shell under uniaxial loading with a circular hole is obtained intuitively with the use of a stress function. A good agreement is obtained for the stresses around and ahead of the circular hole in  $(0 \text{ deg} \pm 30 \text{ deg})_s$  and  $90 \text{ deg}$  laminates with the finite element results. [DOI: 10.1115/1.1320452]*

## Introduction

Prediction of failure strength of brittle laminate with a hole was very well established based on the W-N fracture criteria ([1–4]). Failure of the laminate occurs when the dominant stress near the hole or the average of the dominant stress over a region near the hole reaches the strength of the laminate. Konish and Whitney [5] developed an analytical solution for the stress distribution near a hole in an orthotropic plate. For the shell-type composite structures one has to essentially go for the finite element approach as there is no such analytical solution available in the literature for employing the W-N criteria. For the best numerical results a clear

understanding of the maximum stress location is very essential. Unlike in metallic structures, for fiber-reinforced orthotropic shells, the maximum stress does not occur at the hole edge in a plane normal to the loading direction, but depends on the fiber orientations ([5]). Moreover, establishing convergence for the finite element model for the isotropic medium for a known problem does not ensure convergence for the orthotropic medium. Hence an analytical solution that can bring out the overall behavior of the orthotropic structure is very much required.

Savin [6] in his complex variable approach to the problem of stresses in an isotropic circular cylindrical shell with holes showed that the stress state in a shell is a sum of a plate solution and a function of curvature effect. Konish and Whitney's [5] and Kumar, Rao, and Mathew's [7] orthotropic equations (plate) were based on the sum of an isotropic plate solution and a function of higher order term of distance ahead of the hole in terms of orthotropic material constants. Thus one can conjecture that the orthotropic shell solution in a polar coordinate system  $(\rho, \theta)$  can be obtained as a sum of an isotropic plate equation (first term in (1)), higher order term of distance ahead of a hole (third term in (1)), and functions of isotropic and orthotropic curvature effects (second and fourth terms in (1)).

$$\left. \frac{\sigma_{\theta}^{\text{Sh}}(\rho, \theta)}{\sigma} \right|_{\text{Ortho}} = \left. \frac{\sigma_{\theta}^{\text{Pl}}(\rho, \theta)}{\sigma} \right|_{\text{ISO}} + f(\beta)_{\text{ISO}} + f \left( \begin{array}{l} \text{higher order terms in } \rho \text{ with} \\ \text{orthotropic coefficients} \end{array} \right) + f \left( \begin{array}{l} \text{higher order terms in } \rho \text{ with} \\ \text{orthotropic coefficients for } \beta \end{array} \right) \quad (1)$$

In the present work an analytical solution for the tangential stress distribution ahead of a circular hole in an orthotropic circular cylindrical shell under axial loading is obtained for use via the W-N criteria.

## Analytical Solution for the Tangential Stress Distribution

The most general solution for the stress distribution near cut-outs of any arbitrary shape under tension or internal pressures up to an accuracy of  $\beta^2$  was given by Pirogov [8]. The equation with unknown coefficients (like  $A_0, B_0, E_K, F_K$ , etc.) is of the form

$$\text{Im}(\phi_j) = \frac{1}{\pi} \left\{ \begin{array}{l} \left[ 2A_0^{(j)} \ln \left( \frac{\gamma\beta}{\sqrt{2}} \right) + \left( A_2^{(j)} + \frac{B_2^{(j)}}{\rho^2} \right) \cos 2\theta \right] + \sum_{k=4,6,\dots}^{\infty} \left( \frac{k-2}{2\rho^{k-2}} A_k^{(j)} + \frac{B_k^{(j)}}{\rho^k} \right) \cos k\theta \\ + \beta^2 \left\{ \begin{array}{l} \left[ 2B_0^{(j)} \ln \left( \frac{\gamma\beta}{\sqrt{2}} \right) - \frac{\pi}{4} (2A_0^{(j)} + A_2^{(j)}) \rho^2 + \sum_{k=4,6,\dots}^{\infty} \left( \frac{E_k^{(j)}}{\rho^{k-2}} + \frac{F_k^{(j)}}{\rho^k} \right) \cos k\theta \right] \\ + \left[ \frac{-\pi}{4} (A_0^{(j)} + A_2^{(j)}) \rho^2 + E_2^{(j)} + \frac{F_2^{(j)}}{\rho^2} \right] \cos 2\theta \end{array} \right\} \end{array} \right\} \quad (2)$$

Based on the above stress function, Savin obtained the tangential stress distribution around a circular hole of radius "a" in an

isotropic shell of radius "R" and thickness "t," under axial loading, as a sum of an isotropic plate solution  $(\sigma_{\theta}^{\text{Pl}}(\rho, \theta)/\sigma)$  and a function of isotropic curvature parameter,  $\beta$ . The solution is valid for a hole whose projected size (on a plane passing through the axis of shell and normal to the axis of hole) is close to the actual hole size.

Contributed by the Applied Mechanics Division of THE AMERICAN SOCIETY OF MECHANICAL ENGINEERS for publication in the ASME JOURNAL OF APPLIED MECHANICS. Manuscript received by the ASME Applied Mechanics Division, May 4, 1999; final revision, May 25, 2000. Associate Editor: J. W. Ju.

$$\left. \frac{\sigma_{\theta}^{Sh}(\rho, \theta)}{\sigma} \right|_{ISO} = \frac{1 - \cos 2\theta}{2} + \frac{1}{2\rho^2} - \frac{3}{2\rho^4} \cos 2\theta \quad (= \text{isotropic plate solution}) - \frac{\pi\beta^2}{8} \left( 1 + \frac{3}{\rho^4} \right) \cos 2\theta \quad (= \text{function in isotropic } \beta, f(\beta)_{ISO}). \quad (3)$$

Similarly for an orthotropic shell,

$$\left. \frac{\sigma_{\theta}^{Sh}(\rho, \theta)}{\sigma} \right|_{Ortho} = \left. \frac{\sigma_{\theta}^{Pl}(\rho, \theta)}{\sigma} \right|_{Ortho} + f(\beta)_{Ortho} \quad (4)$$

where  $\beta_{Ortho} = [\sqrt[4]{3(1-\nu^2)(E_{\theta}/E_Y)/2}]a/\sqrt{Rt}$ ,  $\nu$  = Poisson's ratio,  $E_{\theta}$  and  $E_Y$  are the moduli of elasticity in  $\theta$  and  $Y$  (loading direction) directions ([9]), and  $(\sigma_{\theta}^{Pl}(\rho, \theta)/\sigma)$  for the orthotropic plate is available in Kumar et al. [7].

$$\left. \frac{\sigma_{\theta}^{Pl}(\rho, \theta)}{\sigma} \right|_{Ortho} = \frac{1 - \cos 2\theta}{2} + \frac{1}{2\rho^2} - \frac{3}{2\rho^4} \cos 2\theta + \sum_{j=2}^{\infty} \frac{-C_{2j}}{2} \left[ \frac{4j-3}{\rho^{4j-2}} - \frac{4j-1}{\rho^{4j}} \right] \cos 2j\theta \quad (5)$$

Details of the orthotropic coefficients  $C_{2j}$  ( $j$  varying from 1 to  $\infty$ ) are given in the Appendix.

It can be noticed from Pirogov's stress function given in (1) that the higher order terms for the plate solution and  $\beta$  are of similar trigonometric relationship. Therefore, the functions of  $\beta$  may be expressed as

$$f(\beta)_{Ortho} = -\frac{\pi\beta^2}{2} \left\{ \frac{1}{4} \left( 1 + \frac{3}{\rho^4} \right) \cos 2\theta + \sum_{j=2}^{\infty} \frac{C_{2j}}{2} \left[ \frac{4j-3}{\rho^{4j-2}} - \frac{4j-1}{\rho^{4j}} \right] \cos 2j\theta \right\}. \quad (6)$$

Thus the final expression for the tangential stress distribution for an orthotropic circular cylindrical shell with a circular hole is given by

$$\left. \frac{\sigma_{\theta}^{Sh}(\rho, \theta)}{\sigma} \right|_{Ortho} = \frac{1 - \cos 2\theta}{2} + \frac{1}{2\rho^2} - \frac{3}{2\rho^4} \cos 2\theta - \frac{\pi\beta^2}{8} \times \left\{ \left( 1 + \frac{3}{\rho^4} \right) \cos 2\theta \right\} + \left( 1 + \frac{\pi\beta^2}{2} \right) \times \left\{ \sum_{j=2}^{\infty} \frac{-C_{2j}}{2} \left[ \frac{4j-3}{\rho^{4j-2}} - \frac{4j-1}{\rho^{4j}} \right] \cos 2j\theta \right\}. \quad (7)$$

In this work, circular cylindrical shells with  $(0_4, \pm 30)_S$  and  $(90)_{12}$  lay ups made of high modulus M55J/M18 carbon/epoxy laminate having material properties  $E_X = 328.949$  GPa,  $E_Y = 5.955$  GPa,  $G_{XY} = 4.414$  GPa and  $\nu_{XY} = 0.346$ , with layer thickness of 0.1 mm is considered.

### Finite Element Modeling

The laminated circular cylindrical shell ( $R = 48$  mm,  $t = 1.2$  mm and height = 180 mm) with a hole of radius  $a = 5$  mm is modeled using eight-noded layered shell elements available in NISA2 finite element software. Due to the symmetry, one fourth of the shell (at its half height) is modeled. The region around the hole is modeled with a finer mesh with an element size of one tenth of the hole radius up to  $\rho = 0.5$ , then one fifth up to  $\rho = 1$  and

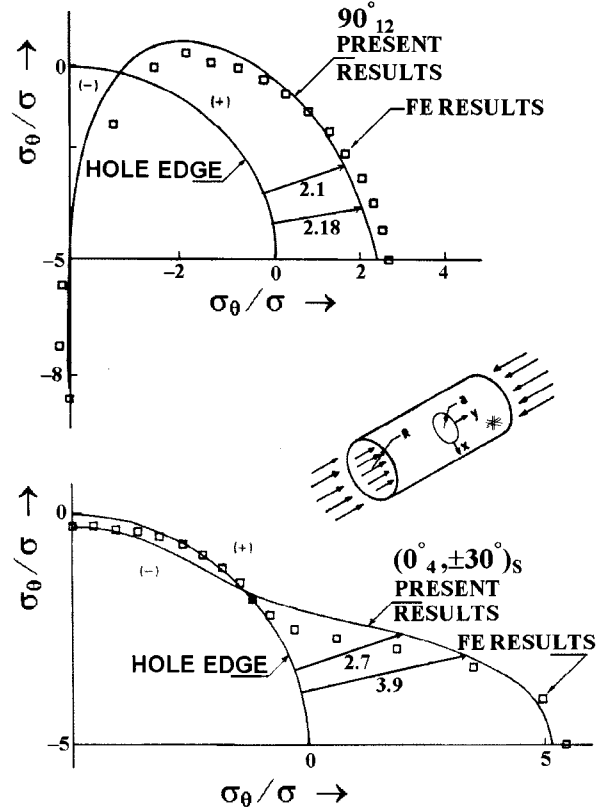


Fig. 1 Tangential stress distribution around a circular hole in an orthotropic shell

then one fourth up to  $\rho = 2$  in the radial direction, while in  $\theta$  direction, it is at every five-degree interval along the circumference of the hole from 0 deg to 180 deg.

**Boundary Conditions.** Symmetric boundary conditions are applied at the symmetric planes.

**Loading.** A distributed load of 240 N is applied on the nodes at the top circumference. The load is distributed in each element in the ratio of 1:4:1 among the nodes in an element.



Fig. 2 Tangential stress distribution ahead of a circular hole in an orthotropic shell

## Results and Discussion

Initially, convergence of (7) is established by progressively increasing the number of terms till a converged value is obtained. For the present cases terms up to  $C_{22}$  ( $j=11$ ) are needed to achieve convergence within one percent. It may be noted that for  $\beta=0$ , (7) reduces to the orthotropic plate solution.

Using (7), the tangential stress distribution around a hole ( $\rho=1$ ) is obtained and compared with the finite element results as shown in Fig. 1. The maximum stress concentration factor of  $-8.56$  is observed at  $\theta=0$  for  $(90)_{12}$  laminate, as against the finite element result of  $-8.71$ . The deviation in the results is estimated as two percent.

In the case of  $(0_4, \pm 30)_S$  lay up, the peak stress occurs at  $\theta=90$  deg as expected, with a stress concentration factor value equal to 5.18 as against the finite element result of 5.44. It can be noticed that the deviation between the two values is about five percent. The stress distributions away from the hole for  $\rho=1$  to 2, for the two types of lay-up sequence considered are shown in Fig. 2. From the finite element analysis, it is found that as a percentage of total stress, bending stress constitute within two percent for the types of lay-up sequences considered. It is concluded that the present solution shows a reasonably good agreement with the finite element results.

## Conclusion

A new analytical solution for tangential stress distribution for an orthotropic circular cylindrical shell with a circular hole under axial loading is derived which gives good agreement with finite element results. The solution can be used with W-N criteria for the prediction of notched strength of an orthotropic shell with a circular hole.

## Appendix

There is a standard technique ([10]) for determining the Fourier coefficients  $C_{2j}$  of a function as in (7):

$$A_0 C_0 + A_2 C_2 + A_4 C_4 = 2a_0 \quad (A1a)$$

$$A_2 C_0 + (A_4 + 2A_0) C_2 + A_2 C_4 + A_4 C_6 = 2a_2 \quad (A1b)$$

and for  $j>3$  a recursive relationship exists in the form

$$C_{2j} = \frac{-1}{A_4} [A_2 C_{2j-2} + 2A_0 C_{2j-4} + A_2 C_{2j-6} + A_4 C_{2j-8}] \quad (A1c)$$

where  $a_0 = 4k(n+k-1)$ ;  $a_2 = -4k(n+k+1)$ ;  $A_0 = 3+n^2-2k+3k^2$

$$A_2 = 4(1-k^2); \quad A_4 = (1-n^2+2k+k^2) \quad (A2)$$

$$n = N/K, \quad N = \sqrt{2(K - \bar{\nu}_{XY}) - \bar{E}_X / \bar{G}_{XY}}$$

$$k = 1/K, \quad K = \sqrt{\bar{E}_X / \bar{E}_Y}$$

$\bar{E}_X, \bar{E}_Y, \bar{\nu}_{XY}, \bar{G}_{XY}$  are the overall orthotropic properties of the shell.

## References

- [1] Whitney, J. M., and Nuismer, R. J., 1974, "Stress Fracture Criteria for Laminated Composites Containing Stress Concentrations," J. Compos. Mater., **8**, pp. 253-265.
- [2] Rhodes, M. D., Mikulas, M. M., and McGowen, P. E., 1984, "Effect of Orthotropy and Width on Compression Strength of Graphite-Epoxy Panels With Holes," AIAA J., **22**, pp. 1283-1292.
- [3] Awerbuch, J., and Madhukar, M. S., 1985, "Notched Strength of Composite Laminates: Prediction and Experiments—A Review," J. Reinf. Plast. Compos., **4**, pp. 3-159.
- [4] Kumar, R. R., 1993, "Experimental Investigation and Prediction on Notched Strength of Laminated Composite Circular Cylindrical Shells," DLR report IB 131-93/16, Germany.
- [5] Konish, H. J., and Whitney, J. M., 1975, "Approximate Stresses in an Orthotropic Plate Containing a Circular Hole," J. Compos. Mater., **9**, pp. 157-166.

- [6] Savin, G. N., 1970, "Stress Distribution Around Holes," NASA Technical Translation, NASA TTF-607.
- [7] Kumar, R. R., Rao, G. V., and Mathew, K. J., 1999, "A New Solution for Prediction of Notched Strength for Highly Orthotropic Plate," J. Aeronaut. Soc. India, **51**, No. 1, pp. 28-34.
- [8] Pirogov, I. M., 1962, "On Approximate Solution of Basic Differential Equations in the Theory of Shells," Izv. Vuzov. Mash, **11**.
- [9] Lekhnitskii, S. G., 1947, *Anisotropic Plates*, Gordon and Breach, New York.
- [10] Krylov, V. I., and Kruglikova, L. G., 1969, *Handbook of Numerical Harmonic Analysis*, Israel Program for Scientific Translations, Jerusalem.

## Stress Wave Propagation in a Coated Elastic Half-Space due to Water Drop Impact

Hyun-Sil Kim<sup>1</sup>

e-mail: hskim@kimm.re.ir

Jae-Seung Kim

Mem. ASME

Hyun-Ju Kang

Sang-Ryul Kim

Acoustics Lab, Korea Institute of Machinery and Materials, Yusong, Taejon 305-600, Korea

*Stress wave propagation in a coated elastic half-space due to water drop impact is studied by using the Cagniard-de Hoop method. The stresses have singularity at the Rayleigh wavefront whose location and singular behavior are determined from the pressure model and independent of the coating thickness, while reflected waves cause minor changes in amplitudes.*  
[DOI: 10.1115/1.1352060]

## Introduction

High-speed impact of liquid drops has been known to cause damage and erosion of the structures such as steam turbine blades, skin of the aircraft, and missiles. Evans et al. [1] used a FDM in studying motion of the elastic bodies, where their pressure loading was obtained as if the water drop collided against a solid surface. Adler [2] performed a more comprehensive three-dimensional finite element method analysis by allowing interactions between a water drop and a deformable target. Blowers [3] studied stress wave propagation in an elastic half-space analytically by employing the Cagniard-de Hoop method ([4]). Although Blowers used a simplified pressure model, which is valid only in the early stage of the impact, his results provided important information about the role of the Rayleigh waves and later his method has been used extensively by others ([5]) to compute the stresses for various materials.

For damage and erosion protection, an idea of coating the surface with a thin elastic layer ([6]) has been frequently used. In order to select the proper coating material and thickness, it is essential to know the stresses inside the coating and the base material. In this paper, we study stress wave propagation in a coated elastic half-space analytically by using the generalized ray

<sup>1</sup>To whom correspondence should be addressed.

Contributed by the Applied Mechanics Division of THE AMERICAN SOCIETY OF MECHANICAL ENGINEERS for publication in the ASME JOURNAL OF APPLIED MECHANICS. Manuscript received by the ASME Applied Mechanics Division, Jan. 27, 1999; final revision, July 21, 2000. Associate Editor: A. K. Mal.

method ([4]). We use the same pressure model as Blowers, which means that our solution is useful only in early stage of the impact process before lateral outflow jetting takes place. However, the results are of great importance, since high stresses and possible damages may occur in a very early stage of the impact.

### Theory

As shown in Fig. 1, we consider a coated elastic half-space ( $z > 0$ ), where a thin elastic layer of uniform thickness  $h$  lies over the surface. On the surface, the stress generated by a water drop impact is given in a cylindrical coordinate by

$$\sigma_{zz}(r, z, t) = -P, \quad r < k_0 \sqrt{t}, \quad \sigma_{zz}(r, z, t) = 0, \quad r > k_0 \sqrt{t}, \quad (1)$$

where  $P$  is a constant pressure and  $k_0$  is a constant determined from the diameter and impact velocity of the water drop ([5]).

The potential functions in the coating and half-space satisfy the wave equations

$$\nabla^2 \phi_i = \frac{1}{\alpha_i^2} \frac{\partial^2 \phi_i}{\partial t^2}, \quad \nabla^2 \psi_i = \frac{1}{\beta_i^2} \frac{\partial^2 \psi_i}{\partial t^2}, \quad (2)$$

where the subscript  $i=1$  is for coating, while  $i=2$  for the half-space. The parameters  $\alpha_i$  and  $\beta_i$  are the sound speeds of P and S waves in the  $i$ th medium. We nondimensionalize the parameters in a similar way as Blowers [3] did, and transform the wave equations by applying the Laplace and Hankel transform with respect to the nondimensionalized time  $T$  and radial distance  $R$ . In the coating, the solution consists of upgoing and downgoing waves due to the reflections at the interface and free surface, while in the half-space the solution contains only downgoing waves. The unknown coefficients can be determined from the boundary conditions.

We show, for instance, the Laplace transformed stress  $\bar{S}_{RR}^1$  in the coating

$$\begin{aligned} \bar{S}_{RR}^1 = & \frac{2 \operatorname{Re}}{\pi} \int_0^\infty \int_0^\infty \left[ \left( \frac{\alpha_1^2}{\beta_1^2} - 2 - 2w^2 \right) \right. \\ & \times (D_\alpha^1 e^{-p \eta_{1\alpha} Z} + U_\alpha^1 e^{-p \eta_{1\alpha} (H-Z)}) \\ & + 2w^2 \left( \frac{\eta_{1\beta}}{\zeta} \right) (D_\beta^1 e^{-p \eta_{1\beta} Z} \\ & \left. - U_\beta^1 e^{-p \eta_{1\beta} (H-Z)}) \right] e^{iRpw} p^4 dw dq, \quad (3) \end{aligned}$$

where  $D_\alpha^1, D_\beta^1, U_\alpha^1, U_\beta^1$  are the coefficients to be determined from the boundary conditions,  $Z$  and  $H$  are the nondimensionalized depth and coating thickness, and  $p, \zeta$  are the Laplace and Hankel transform variables. The parameters  $\eta_{1\alpha}$  and  $\eta_{1\beta}$  are  $\eta_{1\alpha} = \sqrt{\zeta^2 + 1}$  and  $\eta_{1\beta} = \sqrt{\zeta^2 + \alpha_1^2/\beta_1^2}$ .

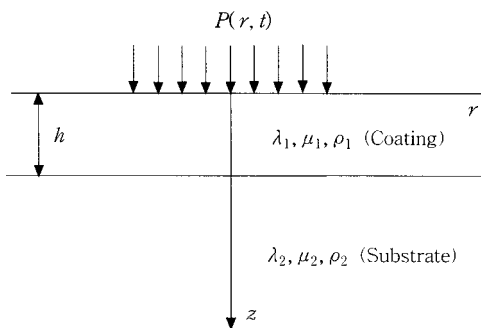


Fig. 1 A coated elastic half-space subject to water drop impact

It can be shown that the coefficients  $D_\alpha^1, D_\beta^1, U_\alpha^1, U_\beta^1$  are expressed in terms of the infinite series, whose physical meaning is that the solution in the coating is composed of the reflected waves and the number of reflections can increase infinitely. The typical form  $\bar{I}_k$  of the infinite series in the stress  $\bar{S}_{RR}^1$  can be expressed as

$$\bar{I}_k = \operatorname{Re} \int_0^\infty \int_0^\infty R_k(w, q) e^{-pg_k(w, q)} dw dq, \quad (4)$$

where  $R_k(w, q)$  and  $g_k(w, q)$  are independent of the variable  $p$ , and  $g_k$  is of the form

$$g_k(w, q) = w^2 + q^2 - iwR + \sum_n b_n \sqrt{w^2 + q^2 + \alpha_1^2/c_n^2}, \quad (5)$$

in which  $c_n$  is  $\alpha_i$  or  $\beta_i$ .

In order to apply the Cagniard-de Hoop method, we deform the integration path such that  $g_k(w, q) = T$ . The new integration path  $w = w(T, q)$  intersects the imaginary  $w$ -axis at  $w = i\nu_m$ . We perform the integration along the new path in  $T$  and change the order of integration to find the inverse Laplace transform as

$$I_k(T) = \operatorname{Re} \left[ \int_0^{q_m} R_k(w, q) \frac{\partial w}{\partial T} dq \right] H(T - T_m(0)), \quad (6)$$

where  $q_m$  and  $T_m$  satisfy the relation,  $T_m(q_m) = T$ , and  $H(T)$  denotes a Heaviside step function. After summation of  $I_k(T)$  over the rays, we can compute the stresses. Depending on the relative positions of  $w = i\nu_m$  and the branch points, we may have to introduce additional integration path to detour the branch cut, which leads to the head wave.

When  $Z=0$ , we need to include the Rayleigh surface wave

$$I_R(T) = D_R \frac{H(T + a^2 - aR)}{\sqrt{(T + a^2)^2 - a^2 R^2}}, \quad (7)$$

where  $D_R$  is the coefficient associated with the residue term and  $a = \alpha_1/c_R$ , in which  $c_R$  is the Rayleigh wave speed in the coating. The surface wave in Eq. (7) has singularity at  $R = (T + a^2)/a$ .

### Numerical Example

For a numerical example, we consider a case that the diameter and velocity of the water drop are  $d_0 = 2$  mm,  $V_0 = 453$  m/s, and the thickness of the coating is  $43 \mu\text{m}$ . The material properties of the coating are: Young's modulus  $E_1 = 1.71 \times 10^{11}$  N/m<sup>2</sup>,  $\alpha_1$

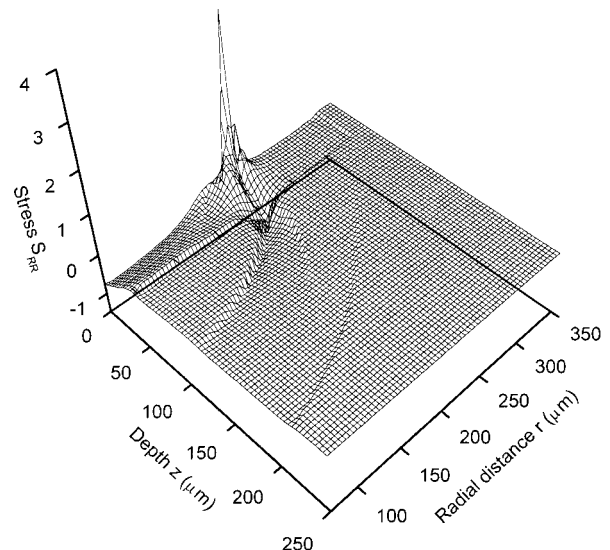
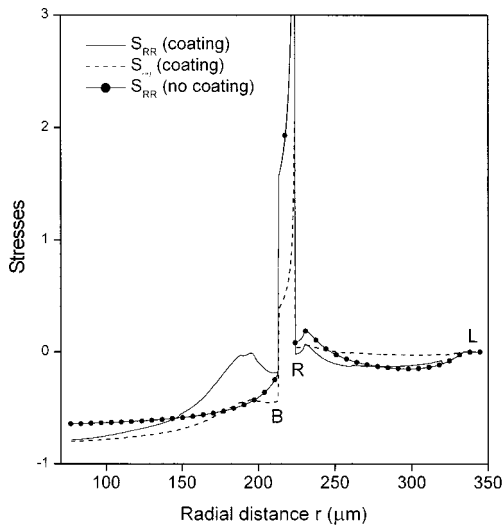


Fig. 2 Snapshot of the stress  $S_{RR}$  when  $t = 0.05 \mu\text{s}$



**Fig. 3** Variation of the nondimensional stresses  $S_{RR}$  and  $S_{\theta\theta}$  as functions of the radial distance  $r$  on the surface when  $t = 0.05 \mu\text{s}$ . Solid line with marks is  $S_{RR}$  when there is no coating and the substrate is filled with the same material as coating.

$= 5910 \text{ m/s}$ ,  $\beta_1 = 3160 \text{ m/s}$ , density  $\rho_1 = 6590 \text{ kg/m}^3$ ; for substrate,  $E_2 = 6.74 \times 10^{10} \text{ N/m}^2$ ,  $\alpha_2 = 4150 \text{ m/s}$ ,  $\beta_2 = 2220 \text{ m/s}$ ,  $\rho_2 = 5270 \text{ kg/m}^3$ . The substrate material is Zinc-Selenide. In Blowers' paper, the only specified material property is Poisson's ratio  $\nu$ , and we use the same value here as  $\nu = 0.3$  for both coating and substrate, for which case  $a = 2.017$ .

In Fig. 2, we plot a snapshot of the nondimensional stress  $S_{RR}$  at  $0.05 \mu\text{s}$ . There is a sharp peak near the surface, which corresponds to the Rayleigh wavefront at  $r = 224 \mu\text{m}$  ( $R = (T + a^2)/a = 5.84$ ). The boundary of the impact is  $r = 213 \mu\text{m}$  ( $R = 2\sqrt{T} = 5.56$ ). In Fig. 3, we show the stresses  $S_{RR}$  and  $S_{\theta\theta}$  at the surface as functions of the radial distance, in which the symbols "B," "R," and "L" mean the boundary of impact area, Rayleigh wavefront, and longitudinal wavefront, respectively. For comparison, we also show the stress  $S_{RR}$  when there is no coating and the half-space is filled with the same material as the coating.

### Concluding Remarks

It was shown that the pressure model in Eq. (1) produces an annular strip of the high tensile stresses outside the contact area due to the Rayleigh wave, which has been observed experimentally by Hand et al. [7]. The location and singular behavior of the Rayleigh wavefront are determined from the pressure model and independent of the coating thickness. The region directly under the contact area is in pure compression. Since the stresses cannot have infinite magnitude in real impact situations, the singularity in the present study may be due to the abrupt change of pressure model at the impact boundary.

### Acknowledgment

The authors would like to thank the Ministry of Science and Technology, Korea, for the financial support by a grant from the Critical Technology 21 Project.

### References

- [1] Evans, A. G., Ito, Y. M., and Rosenblatt, M., 1980, "Impact Damage Thresholds in Brittle Materials Impacted by Water Drops," *J. Appl. Phys.*, **51**, No. 5, pp. 2473–2482.
- [2] Adler, W. F., 1995, "Waterdrop Impact Modeling," *Wear*, **186–187**, pp. 341–351.
- [3] Blowers, R. M., 1969, "On the Response of an Elastic Solids to Droplet Impact," *J. Inst. Math. Appl.*, **5**, No. 2, pp. 167–193.

- [4] van der Hijden, J. H., 1987, *Propagation of Transient Elastic Waves in Stratified Anisotropic Media*, North-Holland, Amsterdam.
- [5] Adler, W. F., 1977, "Liquid Drop Collisions on Deformable Media," *J. Mater. Sci.*, **12**, pp. 1253–1271.
- [6] Springer, G. S., 1976, *Erosion by Liquid Impact*, John Wiley and Sons, New York.
- [7] Hand, R. J., Field, J. E., and Townsend, D., 1991, "The Use of Liquid Jets to Simulate Angled Drop Impact," *J. Appl. Phys.*, **70**, No. 11, pp. 7111–7118.

## Closed-Form Representation of Beam Response to Moving Line Loads

Lu Sun

Department of Civil Engineering, The University of Texas at Austin, ECJ Hall 6.10, Austin, TX 78712  
e-mail: lusun@mail.utexas.edu

Fourier transform is used to solve the problem of steady-state response of a beam on an elastic Winkler foundation subject to a moving constant line load. Theorem of residue is employed to evaluate the convolution in terms of Green's function. A closed-form solution is presented with respect to distinct Mach numbers. It is found that the response of the beam goes to unbounded as the load travels with the critical velocity. The maximal displacement response appears exactly under the moving load and travels at the same speed with the moving load in the case of Mach numbers being less than unity. [DOI: 10.1115/1.1352064]

### 1 Introduction

The response of beams to moving loads has been studied extensively over the past several decades (Fryba [1]). The investigation of Bernoulli-Euler beams with moving loads includes the work of Kenney [2], Steele [3], Huang [4], Choros and Adams [5], Jezequel [6], Elattary [7], Lee [8], Sun and Deng [9], Sun [10], Sun and Greenberg [11], and Benedetti [12]. It is found that the moving load is often treated as a concentrated load. Since the concentrated loading condition is only an idealized model of the tire load, it is preferable to use a distributed line load model to characterize the wheel load more realistically.

Denote  $y(x, t)$  as the deflection of the beam in  $y$ -direction, in which  $x$  represents the traveling direction of the pavement structure, and  $t$  represents time. The well-known governing equation of a Bernoulli-Euler beam on a Winkler foundation is (Sun [10])

$$EI \frac{\partial^4 y}{\partial x^4} + Ky + m \frac{\partial^2 y}{\partial t^2} = P \frac{H[r_0^2 - (x - vt)^2]}{2r_0} \quad (1)$$

where  $EI$  is the rigidity of the beam,  $E$  is Young's modulus of elasticity,  $I$  is the moment of inertia of the beam,  $K$  is the modulus of subgrade reaction,  $m$  is the unit mass of the beam,  $r_0$  is the half-width of the line load,  $P$  is the magnitude of the applied load, and  $H(\cdot)$  is the Heaviside step function.

The Green's function of the beam is defined as the solution of Eq. (1) given that the right-hand side external load is characterized by  $\delta(x - x_0)\delta(t - t_0)$ . Taking two-dimensional Fourier transform and inverse on both sides of Eqs. (1) gives the Green's function

Contributed by the Applied Mechanics Division of THE AMERICAN SOCIETY OF MECHANICAL ENGINEERS for publication in the ASME JOURNAL OF APPLIED MECHANICS. Manuscript received and accepted by the ASME Applied Mechanics Division, Jan. 25, 2000; final revision, Oct. 26, 2000. Associate Editor: A. K. Mal.

$$G(x,t;x_0,t_0) = (2\pi)^{-2} \int_{-\infty}^{\infty} \int_{-\infty}^{\infty} \frac{\exp\{i[\xi(x-x_0) + \omega(t-t_0)]\}}{EI\xi^4 + K - m\omega^2} \times d\xi d\omega. \quad (2)$$

The solution of (1) given  $F(x,t)$  is given by  $y(x,t) = \int_{-\infty}^{\infty} \int_{-\infty}^{\infty} F(x_0,t_0)G(x,t;x_0,t_0)dx_0dt_0$ . Substituting Eqs. (1) and (2) into it gives

$$y(x,t) = \frac{\bar{P}}{2\pi} \int_{-\infty}^{\infty} \frac{\sin r_0 \xi \exp[i\xi(x-vt)]}{r_0 \xi (\xi^4 - \bar{m}v^2 \xi^2 + \bar{K})} d\xi \quad (3)$$

where  $\bar{P} = P/EI$ ,  $\bar{K} = K/EI$  and  $\bar{m} = m/EI$ .

## 2 Closed-Form Representation of the Solution

Expression (3) can be further developed using complex function theory. To do so, one needs to identify the roots of the characteristic equation of this type  $\xi^4 + \bar{K} - \bar{m}v^2 \xi^2 = 0$ . Define a new variable  $u = \xi^2$  so we have a quadratic equation

$$u^2 - \bar{m}v^2 u + \bar{K} = 0. \quad (4)$$

Denote the critical velocity as  $v_{\text{critical}} = (4\bar{K}/\bar{m}^2)^{1/4}$ . Define dimensionless velocity (i.e., the Mach number)  $M = v/v_{\text{critical}}$ .

(a) Subsonic case ( $M < 1$ ).

Two roots of Eq. (4) are  $u_1 = [\bar{m}v^2(1 + i\sqrt{M^{-4}-1})]/2$  and  $u_2 = [\bar{m}v^2(1 - i\sqrt{M^{-4}-1})]/2$ . Further, we have four complex valued roots  $\xi_{1,2} = (\bar{m}v^2/2M^2)^{1/2} \exp[i(2j\pi + \theta)/2]$  and  $\xi_{3,4} = (\bar{m}v^2/2M^2)^{1/2} \exp[i(2j\pi - \theta)/2]$  in which  $\tan \theta = (M^{-4}-1)$  and  $j=0$  and 1. In the case of  $x-vt \geq 0$ , we select the closed contour in the upper half  $\xi$ -plane and, if  $x-vt < 0$ , in the lower half  $\xi$ -plane. To shorten the length of the paper, only the case  $x-vt \geq 0$  is considered in the following. Applying the theorem of residue we obtain

$$y(x,t) = \frac{P}{2\pi EI r_0} \left\{ 2\pi i \sum_{\text{Im } \xi > 0} \text{res} \left\{ \frac{\sin r_0 \xi \exp[i\xi(x-vt)]}{\xi(\xi^4 - \bar{m}v^2 \xi^2 + \bar{K})} \right\} + \pi i \sum_{\text{Im } \xi = 0} \text{res} \left\{ \frac{\sin r_0 \xi \exp[i\xi(x-vt)]}{\xi(\xi^4 - \bar{m}v^2 \xi^2 + \bar{K})} \right\} \right\}. \quad (5)$$

After identifying the residues in Eq. (5), it is straightforward to see

$$y(x,t) = \frac{iP}{EI r_0} \sum_{l=1,4} \frac{\sin r_0 \xi_l \exp[i\xi_l(x-vt)]}{5\xi_l^4 - \bar{m}v^2 \xi_l^2 + \bar{K}}. \quad (6)$$

(b) Sonic case ( $M = 1$ ).

In this case two duplicated roots of Eq. (5) are  $u_{1,2} = \bar{m}v^2/2$ . Thus four real valued roots  $\xi_{1,2} = \xi_{3,4} = \pm(\bar{m}v^2/2)^{1/2}$ . Since these two poles are of the second order, this means that a singularity occurs when integrating (4) along the contour. Using the same procedure as in the case of  $M < 1$ , it is found that dynamic response in this case becomes infinite and the singularity is of the order  $O(\varepsilon^{-1})$ . This result indicates the existence of a resonance phenomenon as  $v = v_{\text{critical}}$ .

(c) Supersonic case ( $M > 1$ ).

Two roots of Eq. (4) are  $u_1 = [\bar{m}v^2(1 + \sqrt{1-M^{-4}})]/2$  and  $u_2 = [\bar{m}v^2(1 - \sqrt{1-M^{-4}})]/2$ . Therefore, we have real valued roots  $\xi_{1,2} = \pm R_1$  and  $\xi_{3,4} = \pm R_2$  where  $R_1 = \{\bar{m}v^2[1 + (1-M^{-4})^{1/2}]/2\}^{1/2}$  and  $R_2 = \{\bar{m}v^2[1 - (1-M^{-4})^{1/2}]/2\}^{1/2}$ . Apparently, since the distribution of the roots of the characteristic equation depends heavily on the range of the Mach number, one may expect that dynamic response of the beam to a moving load will also be distinct for different Mach number.

The poles of a system without damping can be thought of as the limit situation of poles of a system with damping while the damping is approaching zero. The poles of a physical system with tiny damping can be determined by seeking the roots of a new characteristic algebraic equation in which a negative infinitesimal imaginary term is added into the previous characteristic algebraic equation, i.e.,  $\xi^4 - \bar{m}v^2 \xi^2 + \bar{K} - i\varepsilon = 0$  where  $\varepsilon$  is a positive infinitesimal real number. Since  $u = \xi^2$ . This new characteristic equation becomes

$$u^2 - \bar{m}v^2 u + \bar{K} - i\varepsilon = 0. \quad (7)$$

The square root of the discriminant of Eq. (7) is  $\Delta^{1/2} = \bar{m}v^2(1 - M^{-4})^{1/2} \exp(i\psi/2)$ , in which  $\tan \psi = \beta(1-M^{-4})^{-1}$  and  $\beta = 4\bar{m}^{-2}v^{-4}\varepsilon$ . Since  $\beta \rightarrow 0^+$  as  $\varepsilon \rightarrow 0^+$ , we have  $\psi \rightarrow 0^+$  and  $u_1 = 1/2\bar{m}v^2[1 + (1-M^{-4})^{1/2}] \exp(i\lambda_1)$  and  $u_2 = 1/2\bar{m}v^2[1 - (1-M^{-4})^{1/2}] \exp(i\lambda_2)$  as two roots, in which  $\tan \lambda_1 = (1 - M^{-4})^{1/2} \sin \psi/2 / [1 + (1 - M^{-4})^{1/2} \cos \psi/2]$  and  $\tan \lambda_2 = -(1 - M^{-4})^{1/2} \sin \psi/2 / [1 - (1 - M^{-4})^{1/2} \cos \psi/2]$ , respectively. Thus  $\xi_{1,2} = R_1 \exp[i(\lambda_1 + 2j\pi)/2]$  and  $\xi_{3,4} = R_2 \exp[i(\lambda_2 + 2j\pi)/2]$ , ( $j = 0, 1$ ) where  $R_{1,2} = \{\bar{m}v^2[1 \pm (1 - M^{-4})^{1/2}]/2\}^{1/2}$ . Realize  $\lambda_1 = \lim_{\psi \rightarrow 0^+} \arctan(\tan \lambda_1) = 0^+$  and  $\lambda_2 = \lim_{\psi \rightarrow 0^+} \arctan(\tan \lambda_2) = 0^-$ , as  $\psi \rightarrow 0^+$ , the roots  $\xi_1, \xi_2, \xi_3$ , and  $\xi_4$ , respectively, approach their own limits  $\arg \xi_{1,2} = \{\lambda_{1,2}/2\} = \{0^{\pm}\}$  and  $\arg \xi_{3,4} = \{\lambda_{3,4}/2\} = \{0^{\mp}\}$ .

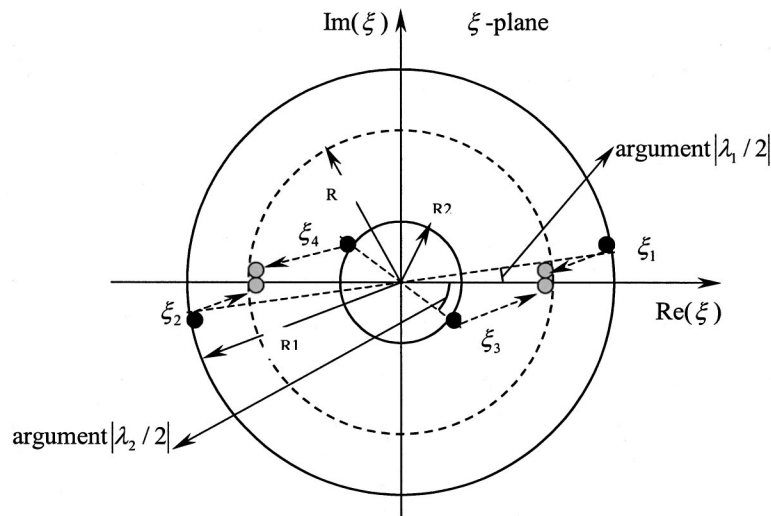


Fig. 1 Poles of the beam on an elastic foundation with tiny amount of damping

Figure 1 depicts the distribution of these poles in the complex  $\xi$ -plane. As  $v$  approaches critical velocity  $v_{\text{critical}}$  (i.e.,  $M \rightarrow 1$ ), four poles (black points) will move towards those poles (gray points) of the case  $v = v_{\text{critical}}$ . Each pair of gray points on one side of the imaginary axis will get more and more close to each other as  $M \rightarrow 1$ , and becomes a single pole of the second order. The dynamic response of the beam is given by

$$y(x,t) = \frac{iP}{2EIr_0} \sum_{l=1,4} \frac{\sin r_0 \xi_l \exp[i\xi_l(x-vt)]}{5\xi_l^4 - \bar{m}v^2 \xi_l^2 + \bar{K}} \quad \text{for } x-vt \geq 0. \quad (8)$$

In the case of  $x-vt < 0$ , we just need to replace  $l = 1, 4$  in Eq. (6) or (8) by  $l = 2, 3$ .

### 3 Maximum Response

Define  $\eta = x - vt$ . The derivative of  $y(x,t)$  with respect to  $\eta$  suggests that  $\eta = 0$  correspond to the extreme point. The maximum response in the case of  $M < 1$  can be obtained by substituting  $x - vt = 0$  into Eq. (7). Define new parameters. The maximum response is  $y_{\text{max}}^{\text{moving}}(x = vt) = iP/EI r_0 \{ \sin[r \exp(i\theta/2)]/S_1 + iW_1 + \sin\{r \exp[i(-\theta + \pi)/2]\}/S_2 + iW_2 \}$  in which  $S_1 = 5\phi^4 \cos 2\theta - 3\bar{m}v^2 \phi^2 \cos \theta + \bar{K}$ ,  $S_2 = 5\phi^4 \cos 2\theta + 3\bar{m}v^2 \phi^2 \cos \theta + \bar{K}$ ,  $W_1 = 5\phi^4 \sin 2\theta - 3\bar{m}v^2 \phi^2 \sin \theta$ , and  $W_2 = 5\phi^4 \sin 2\theta + 3\bar{m}v^2 \phi^2 \sin \theta$ ,  $\phi = (\bar{m}v^2/2M^2)^{1/2}$  and  $r = \phi r_0$ . Using Maclaren series to expand  $y_{\text{max}}^{\text{moving}}(x = vt)$  and taking only the real part

$$y_{\text{max}}^{\text{moving}}(x = vt) = -\frac{P}{EI r_0} \left\{ \frac{A_1 S_1 - B_1 W_1}{S_1^2 + W_1^2} + \frac{A_2 S_2 - B_2 W_2}{S_2^2 + W_2^2} \right\} \quad (9)$$

where

$$A_1 = \sum_{n=0}^{\infty} \frac{(-1)^n r^{2n+1} \sin[\theta(2n+1)/2]}{(2n+1)!},$$

$$B_1 = \sum_{n=0}^{\infty} \frac{(-1)^n r^{2n+1} \cos[\theta(2n+1)/2]}{(2n+1)!},$$

$$A_2 = \sum_{n=0}^{\infty} \frac{r^{2n+1} \cos[\theta(2n+1)/2]}{(2n+1)!} \quad \text{and}$$

$$B_2 = \sum_{n=0}^{\infty} \frac{r^{2n+1} \sin[\theta(2n+1)/2]}{(2n+1)!}.$$

It should be noted that, although  $\eta = 0$  can make  $d/d\eta y = 0$  satisfied, it is a sufficient condition rather than a necessary condition. Actually, the response of the beam at the center of the moving load is the maximal response in the case of  $M < 1$ , while the response of that location remains quiescent in the case of  $M > 1$ . It also should be pointed out that similar method is applicable to moving load problem with damping considered in the governing equation. Given the limit of the content, the result is not presented herein.

### References

- [1] Fryba, L., 1977, *Vibration of Solids and Structures Under Moving Loads*, Noordhoff, Groningen, The Netherlands.
- [2] Kenney, J. T., 1954, "Steady State Vibrations of Beam on Elastic Foundation for Moving Loads," *ASME J. Appl. Mech.*, **21**, pp. 359–364.
- [3] Steele, C. R., 1967, "The Finite Beam With a Moving Load," *ASME J. Appl. Mech.*, **34**, p. 111.
- [4] Huang, C. C., 1977, "Traveling Loads on a Viscoelastic Timoshenko Beam," *ASME J. Appl. Mech.*, **44**, pp. 183–184.
- [5] Choros, J., and Adams, G. G., 1979, "A Steadily Moving Load on an Elastic Beam Resting on a Tensionless Winkler Foundation," *ASME J. Appl. Mech.*, **46**, No. 1, pp. 175–180.
- [6] Jezequel, L., 1981, "Response of Periodic Systems to a Moving Load," *ASME J. Appl. Mech.*, **48**, pp. 613–618.
- [7] Elattary, M. A., 1991, "Moving Loads on an Infinite Plate Strip of Constant Thickness," *J. Phys. D: Appl. Phys.*, **24**, No. 4, 541–546.
- [8] Lee, H. P., 1994, "Dynamic Response of a Beam With Intermediate Point Constraints Subject to a Moving Load," *J. Sound Vib.*, **171**, No. 3, pp. 361–368.

- [9] Sun, L., and Deng, X., 1997, "Transient Response for Infinite Plate on Winkler Foundation by a Moving Distributed Load," *Chin. J. Appl. Mech.*, **14**, No. 2, pp. 72–78.
- [10] Sun, L., 1998, "Theoretical Investigations on Vehicle-Ground Dynamic Interaction," Final Report prepared for National Science Foundation of China, Southeast University, Nanjing, China.
- [11] Sun, L., and Greenberg, B., 2000, "Dynamic Response of Linear Systems to Moving Stochastic Sources," *J. Sound Vib.*, **229**, No. 4, pp. 957–972.
- [12] Benedetti, G. A., 1974, "Dynamic Stability of a Beam Loaded by a Sequence of Moving Mass Particles," *ASME J. Appl. Mech.*, **41**, pp. 1069–1071.

## An Analytic Algorithm of Stresses for Any Double Hole Problem in Plane Elastostatics

Lu-qing Zhang

Engineering Geomechanics Laboratory, Institute of Geology and Geophysics, Chinese Academy of Sciences, Beijing 100029, China

Ai-zhong Lu

Professor, Department of Civil Engineering, Shandong University of Science and Technology, Tai'an 271019, China

*This paper gives an analytic algorithm to plane elastostatic problem of an infinite medium containing two holes of arbitrary shapes and arrangement, using Schwarz's alternating method, and finds that the method has a very quick convergence speed even for solving a complex double hole problem.*

[DOI: 10.1115/1.1352065]

### 1 Introduction

There are a large number of papers in plane elastostatics dealing with regions containing two circular holes ([1–4]). It seems that only Hasebe et al. [5] provided one analysis method for the problem of two complex holes in which one hole is of complex profile and the other is a crack. However, the method is only suitable for a symmetrical double hole problem.

The crucial ingredient in solving a double hole problem by means of Schwarz's alternating method is the repeated solution of a single hole problem, which can be well solved by Muskhelishvili's method ([6]) via a conformal transformation of mapping the given hole shape into a unit circle. The iterative solutions for the Schwarz's alternating method needs many repeated transformations between the physical and mapped planes. In order to conduct the iterative solutions easily, two mapping functions of two holes,  $z_1 = \omega_1(\zeta_1)$  and  $z_2 = \omega_2(\zeta_2)$ , and two corresponding inverse mapping functions,  $\zeta_1 = \omega_1^{-1}(z_1)$  and  $\zeta_2 = \omega_2^{-1}(z_2)$ , are introduced. In the process of iterative solutions every iteration refers to the completion of solutions for two single hole problems.

### 2 Basic Formulas for Stress Analysis of Any Double Hole Problem

In Fig. 1  $z_1$  and  $z_2$  are the complex coordinates in  $x_1 o_1 y_1$  and  $x_2 o_2 y_2$  local coordinate systems, respectively;  $c$  is the relative

Contributed by the Applied Mechanics Division of THE AMERICAN SOCIETY OF MECHANICAL ENGINEERS for publication in the ASME JOURNAL OF APPLIED MECHANICS. Manuscript received by the ASME Applied Mechanics Division, Mar. 22, 2000; final revision, Sept. 20, 2000. Associate Editor: J. R. Barber.

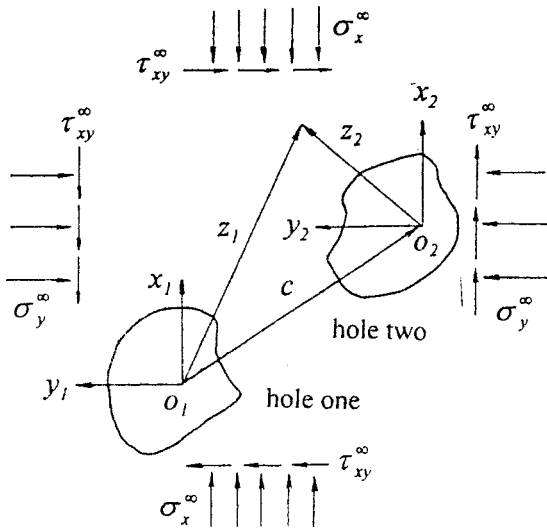


Fig. 1 The calculating model for any double hole problem

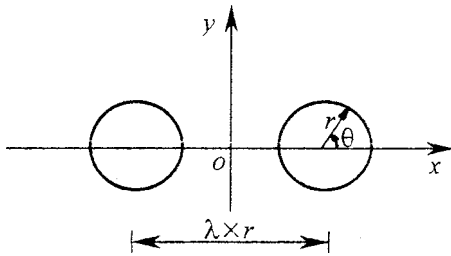


Fig. 2 The problem for two circular holes

position vector of two holes in  $x_1o_1y_1$  coordinate system;  $\sigma_x^\infty$ ,  $\sigma_y^\infty$ , and  $\tau_{xy}^\infty$  are external loads uniformly distributed at infinity.

In the process of the first iteration, the presence of hole one will lead to a single hole problem, whose solution of stresses can be written in terms of two complex stress functions,  $\varphi_{11}(\zeta_1)$  and  $\psi_{11}(\zeta_1)$ , of the complex variable  $\zeta_1$ . The stress boundary condition for the presence of hole one is

$$\varphi_{11}(\sigma_1) + \frac{\omega_1(\sigma_1)}{\omega_1'(\sigma_1)} \overline{\varphi_{11}'(\sigma_1)} + \overline{\psi_{11}(\sigma_1)} = f_1(\sigma_1) \quad (1)$$

where a prime on a function denotes differentiation with respect to its argument, and a bar on a function indicates its conjugate;  $\sigma_1$  is the value of  $\zeta_1$  on the unit circle;  $\varphi_{11}(\sigma_1)$  and  $\psi_{11}(\sigma_1)$  are the values of  $\varphi_{11}(\zeta_1)$  and  $\psi_{11}(\zeta_1)$  on the unit circle, respectively;  $f_1(\sigma_1)$  is the principal vector of surface forces at the edge of hole one.

The stress functions  $\varphi_{11}(\zeta_1)$  and  $\psi_{11}(\zeta_1)$  can be used as the loading functions for solving another single hole problem induced by the presence of hole two. At this stage the boundary conditions are satisfied at the edge of hole one, however, there exist redundant surface forces at the edge of hole two. The redundant surface forces are obtained directly by three coordinate transformations between coordinates  $\zeta_2$ ,  $z_2$ ,  $z_1$  and  $\zeta_1$  and a formula

$$f_{12}(\sigma_2) = \varphi_{11}(\gamma_1) + \frac{\omega_1(\gamma_1)}{\omega_1'(\gamma_1)} \overline{\varphi_{11}'(\gamma_1)} + \overline{\psi_{11}(\gamma_1)} \quad (2)$$

where  $\sigma_2$  is the value of boundary point  $t_2$  of hole two in  $\zeta_2$  plane;  $f_{12}(\sigma_2)$  is the principal vector of the redundant surface forces with respect to  $\sigma_2$ ;  $\gamma_1$  is the coordinate of  $\sigma_2$  in  $\zeta_1$  plane via mapping transformation  $t_2 = \omega_2(\sigma_2)$ , coordinate translation  $T_1 = t_2 + c$  and inverse mapping transformation  $\gamma_1 = \omega_1^{-1}(T_1)$ .

The distribution of  $f_{12}(\sigma_2)$  at the edge of hole two can be approximated by complex series  $\sum_{k=-L}^L D_k \sigma_2^k$ , in which  $D_k$  is the complex coefficient of  $\sigma_2^k$ . In order to eliminate the redundant surface forces, the reversed forces of  $\sum_{k=-L}^L D_k \sigma_2^k$ ,  $-\sum_{k=-L}^L D_k \sigma_2^k$ , are imposed at the edge of hole two, yielding the other single hole problem in the first iteration. The solution for the presence of hole two can be expressed by two complex stress functions  $\varphi_{22}(\zeta_2)$  and  $\psi_{22}(\zeta_2)$ . The corresponding stress boundary condition is

$$\varphi_{22}(\sigma_2) + \frac{\omega_2(\sigma_2)}{\omega_2'(\sigma_2)} \overline{\varphi_{22}'(\sigma_2)} + \overline{\psi_{22}(\sigma_2)} = f_2(\sigma_2) - \sum_{k=-L}^L D_k \sigma_2^k \quad (3)$$

Table 1 The comparison of the maximum tensile stresses at the edge of the right hole from two methods

$\lambda$	solution	all-around unit tension		horizontal unit tension		vertical unit tension	
		$\theta = 0$	$\theta = \pi$	$\theta = +\pi/2$	$\theta = -\pi/2$	$\theta = 0$	$\theta = \pi$
2	exact solution	2.894	$\infty$	2.569	2.569	3.869	$\infty$
	iterative solution	2.659375	35.570570	2.557303	2.557303	3.601490	40.281910
3	exact solution	2.255	2.887	2.623	2.623	3.151	3.264
	iterative solution	2.254839	2.887496	2.623146	2.623145	3.150994	3.264019
4	exact solution	2.158	2.411	2.703	2.703	3.066	3.020
	iterative solution	2.157655	2.410827	2.702637	2.702636	3.066025	3.020181
6	exact solution	2.080	2.155	2.825	2.825	3.020	2.992
	iterative solution	2.080380	2.154591	2.825038	2.825037	3.020114	2.992179
10	exact solution	2.033	2.049	2.927	2.927	3.004	2.997
	iterative solution	2.032807	2.048810	2.926672	2.926672	3.004336	2.996998
16	exact solution	2.014	2.018	2.970	2.970	3.001	2.999
	iterative solution	2.013795	2.017700	2.969799	2.969798	3.001042	2.999149
$\infty$	exact solution	2.000	2.000	3.000	3.000	3.000	3.000
	iterative solution	2.000000	2.000000	3.000000	3.000000	3.000000	3.000000

Note: To see the difference from the exact solution with three decimal numbers, every iterative one is given by six decimal numbers.

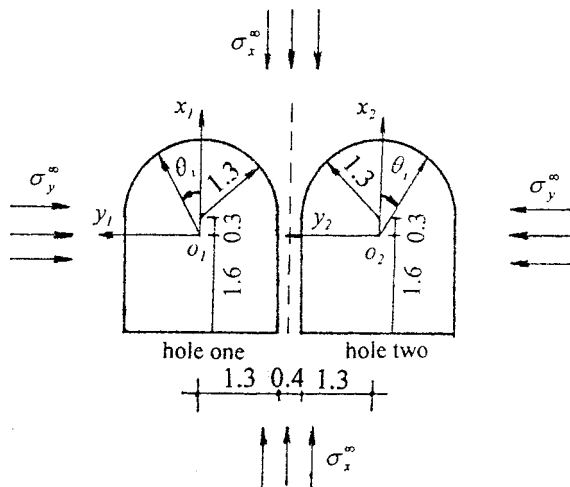


Fig. 3 The problem for two complex holes

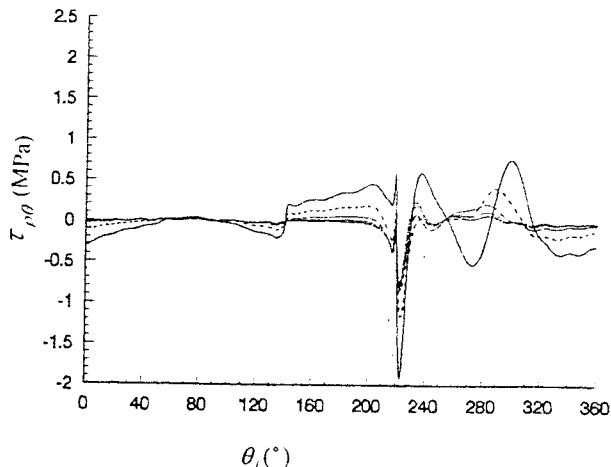
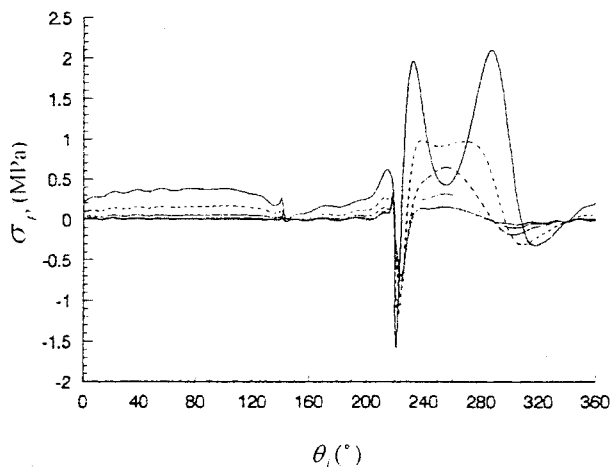
where  $\varphi_{22}(\sigma_2)$  and  $\psi_{22}(\sigma_2)$  are the values of  $\varphi_{22}(\zeta_2)$  and  $\psi_{22}(\zeta_2)$  on the unit circle in  $\zeta_2$  plane, respectively;  $f_2(\sigma_2)$  is the principal vector of surface forces at the edge of hole two.

The superposition of  $\varphi_{11}(\zeta_1)$ ,  $\psi_{11}(\zeta_1)$  and  $\varphi_{22}(\zeta_2)$ ,  $\psi_{22}(\zeta_2)$  is the solution for the first iteration of the Schwarz's alternating method. At this stage, the boundary conditions only at the edge of hole two are satisfied. Of course, the second and later iterations can be operated.

Taking  $\varphi(\zeta)$  and  $\psi(\zeta)$  as the superposition of two stress functions for all required iterative solutions, the stress components can be obtained readily.

### 3 Discussions on the Convergence Accuracy of Iterative Solutions

**3.1 Comparison With the Exact Solution for the Problem of Two Circular Holes.** Now let us consider a linearly elastic medium containing two equal circular holes, as plotted in Fig. 2. Three fundamental loading cases are discussed in some detail, namely, the all-around, horizontal and vertical tensions applied at infinity. Owing to the symmetry of the problem, Table 1 only



— three iterations — — — five iterations — — — — ten iterations — — — — — fifteen iterations — — — — — twenty iterations

Fig. 4 The redundant surface forces  $\sigma_\rho$  and  $\tau_{\rho\theta}$  for different iterations

Table 2 The maximum compressive stresses at the edges of two holes

arrangement	loads	position	hole two		hole one		hole two	
			hole one	hole two	hole one	hole two	hole one	hole two
			$c = 0.0 - 4.0i$		$c = 2\sqrt{2} - 2\sqrt{2}i$		$c = 4.0 + 0.0i$	
$\sigma_x^\infty = 2$ $\sigma_y^\infty = 1$	$\theta = 141^\circ$		14.713	14.722	15.742	13.297	14.181	11.657
	$\theta = 219^\circ$		13.653	13.667	9.724	23.706	14.181	11.657
$\sigma_x^\infty = 1.5$ $\sigma_y^\infty = 1.5$	$\theta = 141^\circ$		14.425	14.436	16.030	10.339	14.978	15.010
	$\theta = 219^\circ$		11.291	11.336	12.446	25.258	14.978	15.010
$\sigma_x^\infty = 1$ $\sigma_y^\infty = 2$	$\theta = 141^\circ$		14.566	14.574	16.817	7.859	16.208	18.801
	$\theta = 219^\circ$		9.538	9.587	15.688	28.087	16.208	18.801

gives the maximum tensile stresses on the boundary of the right hole in which the iterative solutions are obtained by the Schwarz's alternating method for ten iterations and the exact one given by Ling [3].

**3.2 Accuracy Analysis for the Problem of Two Complex Holes.** Let us consider the problem of an infinite and linearly elastic region, containing two complex holes, only under the action of compressive stresses at infinity ( $\sigma_x^\infty = 10$  MPa and  $\sigma_y^\infty = 20$  MPa) (see in Fig. 3). If the solution is terminated at some iteration, the boundary condition of zero surface forces along hole two will be satisfied exactly and along hole one approximately. Figure 4 plots the distribution of redundant surface forces along hole one for 3, 5, 10, 15, and 20 iterative solutions, seen from which the redundant surface forces are gradually reduced to zeroes as the further iteration.

#### 4 The Maximum Stresses Around Two Holes for Different Loads and Arrangements

This paper still takes two holes in Fig. 3 as examples, only changing the loads at infinity and arrangement of the two holes. Three loading cases and three arrangement cases are investigated, and the maximum stresses at the edges of two holes are presented in Table 2.

#### Acknowledgment

This paper is supported by the Chinese National Natural Science Foundation (No. 49772166).

#### References

- [1] Howland, R. C. J., and Knight, R. C., 1939, "Stress Functions for a Plate Containing Groups of Circular Holes," *Philos. Trans.*, **238**, pp. 357–392.
- [2] Green, A. G., 1940, "General Biharmonic Analysis for a Plate Containing Circular Holes," *Proc. R. Soc. London, Ser. A*, **176**, pp. 121–139.
- [3] Ling, Chin-bing, 1948, "On the Stresses in a Plate Containing Two Circular Holes," *J. Appl. Phys.*, **19**, pp. 77–82.
- [4] Ukadgaonker, V. G., 1982, "Stress Analysis of a Plate Containing Two Circular Holes Having Tangential Stresses," *AIAA J.*, **20**, pp. 125–128.
- [5] Hasebe, N., Yoshikawa, K., Ueda, M., and Nakamura, T., 1994, "Plane Elastic Solution for the Second Mixed Boundary Value Problem and Its Application," *Archive of Applied Mechanics*, **64**, pp. 295–306.
- [6] Muskhelishvili, N. I., 1953, "Some Basic Problems of Mathematical Theory of Elasticity," P. Noordhoff, Groningen, The Netherlands.

## The Rotating Tautochrone

### T. J. Osler

Mathematics Department, Rowan University, Glassboro, NJ 08028  
e-mail: osler@rowan.edu

### E. Flores

Chemistry and Physics Department, Rowan University, Glassboro, NJ 08028  
e-mail: flores@rowan.edu

*In a recent paper by Flores and Osler, the authors investigated tautochrone curves in the  $xy$ -plane under an arbitrary potential  $V(y)$ . In this paper we imagine that the  $xy$ -plane of the tautochrone curve is rotating about the  $y$ -axis with constant angular*

*momentum. We find the differential equation of the tautochrone curves. While this differential equation is difficult to solve analytically, several exact solutions (in terms of elementary functions) are obtained in an indirect manner. Intuitive motivation for tautochrone motion is given. [DOI: 10.1115/1.1352066]*

## 1 Introduction

Consider a bead of unit mass that moves on a frictionless wire described by the curve  $x=x(y)$  in the  $xy$ -plane. Assume that the bead starts at time  $t=0$  at the point  $(x(Y), Y)$  with no initial velocity and that the curve  $x=x(y)$  terminates on the  $x$ -axis at the point  $(x_0, 0)$ . The motion of the bead is governed by a potential  $V(y)$  as it moves along the curve  $x=x(y)$ . This curve is called a *tautochrone* if the time  $T$  required for the motion from the starting point at  $(x(Y), Y)$  to the final point  $(x_0, 0)$  is independent of  $Y$ , (the starting height on the curve). The problem of determining the shape of the tautochrone curve under the gravitational potential  $V(y)=gy$  was solved by Huygens and by Abel. The authors studied this problem under arbitrary potentials  $V(y)$  in a recent paper ([1]) using the fractional calculus. In this paper we assume that the  $xy$ -plane containing our curve  $x=x(y)$  is rotating with constant angular momentum  $L$  about a shaft centered on the  $y$ -axis.

In our previous study ([1]) (angular velocity  $\omega=0$ ) we determined that the time  $T$  for the bead to descend from  $y=Y$  to  $y=0$  is given by

$$\int_0^Y \frac{ds}{\sqrt{V(Y)-V(y)}} = \sqrt{2}T. \quad (1)$$

Here  $s$  measures the distance along the curve  $x=x(y)$  starting from  $(x_0, 0)$  to the point  $(x(y), y)$ . Using the fractional calculus we determined that when the curve is a tautochrone, then the potential and the arc length are related by

$$V(y) = \frac{\pi^2}{8T^2} s^2. \quad (2)$$

We also determined that the differential equation satisfied by the tautochrone curve is

$$1 + x'(y)^2 = \frac{2T^2}{\pi^2} \frac{V'(y)^2}{V(y)}. \quad (3)$$

For (3) to be valid, we require that  $V(0)=0$ . (This can always be achieved by simply adding a constant to the potential.) The solution for our tautochrone curve in terms of the given potential is

$$x(y) = \int_0^y \sqrt{\frac{2T^2}{\pi^2} \frac{V'(u)^2}{V(u)} - 1} du + x_0. \quad (4)$$

We will use the above results when we solve our rotating tautochrone problem.

## 2 The Rotating Versus Nonrotating Tautochrones

The sum of the kinetic and potential energies for the rotating parts and for our bead of unit mass on the wire  $x=x(y)$  in the rotating  $xy$ -plane (angular velocity  $\omega(y)$ ) is

$$\begin{aligned} & \frac{1}{2} I \omega(Y)^2 + \frac{1}{2} \omega(Y)^2 x(Y)^2 + V(Y) \\ & = \frac{1}{2} \left( \frac{ds}{dt} \right)^2 + \frac{1}{2} I \omega(y)^2 + \frac{1}{2} \omega(y)^2 x(y)^2 + V(y). \end{aligned} \quad (5)$$

The following are important features of (5):

A The wire and rotating "parts" are rigid and rotating freely (without torque) about the  $y$ -axis. (See Fig. 1.)

B On the left of (5) we see the energy at the moment the bead is released at the point  $(X, Y)$  and on the right we see the energy when the bead is at the arbitrary point  $(x, y)$  on the wire.

Contributed by the Applied Mechanics Division of THE AMERICAN SOCIETY OF MECHANICAL ENGINEERS for publication in the ASME JOURNAL OF APPLIED MECHANICS. Manuscript received by the ASME Applied Mechanics Division, Apr. 2, 2000; final revision, Oct. 9, 2000. Associate Editor: A. A. Ferri.

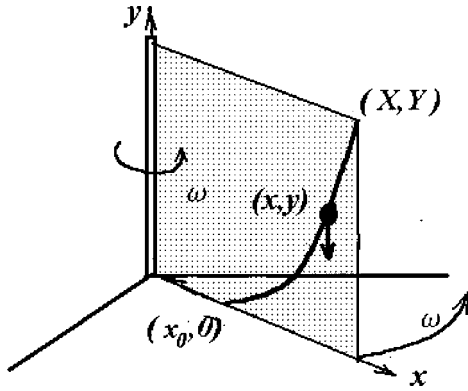


Fig. 1 The rotating frictionless wire with supports

C The wire is given an initial angular velocity and the bead is started with zero velocity relative to the rotating frame. In particular, at time  $t=0$  the system is rotating with angular velocity  $\omega(Y)$  about the  $y$ -axis.

D As a consequence of C, at time  $t=0$  the bead has no component of velocity tangent to the curve but it does have a component of velocity perpendicular to the  $xy$ -plane given by  $\omega(Y)x(Y)$ .

E During the motion the angular velocity of the bead (and the system of parts) given by  $\omega(y)$  will vary. It will change so that angular momentum is always conserved. (See relation (12)).

F The moment of inertia of the wire, rotating shaft and supports is  $I$  and its kinetic energy is the term  $1/2I\omega(y)^2$ .

G The term  $ds/dt$  is the magnitude of the velocity component tangent to the curve. The arc length  $s$  is measured from the terminal point  $(x_0, 0)$  to the moving point  $(x(y), y)$ .

If we call  $V_*(y)$  the terms

$$V_*(y) = V(y) + \frac{1}{2}I\omega(y)^2 + \frac{1}{2}\omega(y)^2x(y)^2, \quad (6)$$

we can abbreviate the writing of (5) as simply

$$V_*(Y) = V_*(y) + \frac{1}{2}\left(\frac{ds}{dt}\right)^2. \quad (7)$$

Solving (7) for  $ds/dt$  we get

$$\frac{ds}{dt} = -\sqrt{2}\sqrt{\{V_*(Y)\} - \{V_*(y)\}}. \quad (8)$$

The minus sign in (8) is due to the assumption that the arc length  $s$  is decreasing. This requires that the initial angular speed  $\omega(Y)$  be small enough that when the bead is released with zero relative velocity, the bead falls downward instead of flying outward. For example, in the case of a gravity-potential, it assumes that

$$\frac{dy}{dx} > \frac{x(Y)\omega(Y)^2}{g}.$$

We can now write

$$\sqrt{2}dt = -\frac{ds}{\sqrt{V_*(Y) - V_*(y)}}. \quad (9)$$

Integrating from the beginning of the motion to the end we get

$$\sqrt{2}T = \int_0^Y \frac{ds}{\sqrt{V_*(Y) - V_*(y)}}. \quad (10)$$

Notice that Eqs. (1) and (10) have the same form, thus, they have the same solution. This implies that for a given curve  $x=x(y)$ , the time  $T$  for the rotating case under the potential  $V(y)$  is the same as the time for the nonrotating case under the potential  $V_*(y)$ . This last statement is important for our work. If we know that the curve

$x=x(y)$  is a nonrotating tautochrone under the potential  $V_*(y)$ , then we know that the same curve is a tautochrone rotating with angular velocity  $\omega(y)$  under the potential

$$V(y) = V_*(y) - \frac{1}{2}(I+x(y)^2)\omega(y)^2. \quad (11)$$

We can eliminate  $\omega(y)$  from (11) by using the conservation of angular momentum expressed as

$$L = (I+x(Y)^2)\omega(Y) = (I+x(y)^2)\omega(y). \quad (12)$$

We require that this angular velocity vary with the starting height  $Y$  so as to keep the angular momentum  $L$  constant.

Solving (12) for  $\omega(y)$  and substituting into (11) we get

$$V(y) = V_*(y) - \frac{1}{2} \frac{L^2}{(I+x(y)^2)}. \quad (13)$$

We recall from our previous paper that all the potentials we use are required to satisfy  $V(0) = V_*(0) = 0$  so that relations (1) to (4) are all valid. Since  $x(0) = x_0$  we must add the constant term  $L^2/2(I+x_0^2)$  to the right side of (13) so that all potentials are zero when  $y=0$ . We get

$$V(y) = V_*(y) - \frac{1}{2} \frac{L^2}{(I+x(y)^2)} + \frac{L^2}{2(I+x_0^2)}. \quad (14)$$

We will use (14) to find several rotating tautochrones in the next section.

### 3 Finding Exact Rotating Tautochrones

In our previous paper we found exact nonrotating tautochrones indirectly. We started with a curve  $x=x(y)$  for which we could calculate the arc length  $s=s(y)$  exactly. We then used relation (2) to find the potential that would make this curve a tautochrone. Nine such curves were selected for their ease of calculation. All nine can be easily modified using (14) to give us rotating tautochrones. The results are shown in Table 1.

While all the resulting potentials are bizarre, we believe it is important to collect exact solutions of mechanics problems whenever they are possible. When exact analytic solutions cannot be found, perturbation or numerical solutions are usually possible. The latter tell us much less than the exact solutions.

### 4 The Differential Equation for the Rotating Tautochrone

We will now find the differential equation satisfied by the rotating tautochrone. Relation (3) is the differential equation for the nonrotating tautochrone. Substituting  $V_*(y)$  from (14) for  $V(y)$  in (3) we get

$$1 + x'(y)^2 = \frac{2T^2}{\pi^2} \frac{\left\{ V'(y) - \frac{L^2x(y)x'(y)}{(I+x(y)^2)^2} \right\}^2}{\left\{ V(y) + \frac{L^2}{2(I+x(y)^2)} - \frac{L^2}{2(I+x_0^2)} \right\}}. \quad (15)$$

This is our differential equation for the rotating tautochrone. It is much more complex and difficult to solve than (3). We can rewrite (15) in the form

$$\pi^2 \{ 2(I+x_0^2)(I+x(y)^2)V(y) - L^2x(y)^2 \} (I+x(y)^2)^3 (1+x'(y)^2) = 4(I+x_0^2)T^2 \{ (I+x(y)^2)V'(y) - L^2x(y)x'(y) \}^2. \quad (16)$$

We can use (15) or (16) to check our solutions in Table 1, but solving exactly for a given potential appears to be difficult. Of course, numerical solutions are possible.

### 5 The Case Where $I$ is Large

We now discuss the approximation where the moment of inertia of the bead,  $x^2$ , is much smaller than  $I$ , the moment of inertia of

**Table 1 Examples of Potentials and Corresponding Rotating Tautochrone Curves**

	Tautochrone Curve	Arc Length $s$	Potential $V(y)$
1	$x = R \sin \theta + x_0$ , $y = R - R \cos \theta$ circle: center $(x_0, R)$ , radius $R$	$s = R\theta = R \cos^{-1}\left(\frac{R-y}{R}\right)$	$\frac{\pi^2 R^2}{8T^2} \left\{ \cos^{-1}\left(\frac{R-y}{R}\right) \right\}^2 + \frac{L^2}{2(I+x_0^2)}$  $-\frac{L^2}{2(I+(\sqrt{2Ry-y^2+x_0})^2)}$
2	$x = R - R \cos \theta + x_0$ $y = R \sin \theta$ circle: center $(R+x_0, 0)$ , radius $R$	$s = R\theta = R \sin^{-1}(y/R)$	$\frac{\pi^2 R^2}{8T^2} \{ \sin^{-1}(y/R) \}^2 + \frac{L^2}{2(I+x_0^2)}$  $-L^2/(2(I+(R-\sqrt{R^2-y^2+x_0})^2))$
3	$x = R \sin(\alpha + \theta) - R \sin \alpha$ $+x_0$ $y = R \cos \alpha - R \cos(\alpha + \theta)$ , $R$ and $\alpha$ fixed circle: radius $R$ center $(x_0 - R \sin \alpha, R \cos \alpha)$	$s = R\theta$ $\theta = \cos^{-1}\left(\frac{R \cos(\alpha) - y}{R}\right) - \alpha$	$\frac{\pi^2 R^2}{8T^2} \left\{ \cos^{-1}\left(\frac{a-y}{R}\right) - \alpha \right\}^2 + \frac{L^2}{2(I+x_0^2)}$  $-\frac{L^2}{2(I+(\sqrt{R^2-(R \cos \alpha - y)^2 - R \sin \alpha + x_0})^2)}$ where $a = R \cos(\alpha)$
4	$x = R(\theta + \sin \theta) + x_0$ $y = R(1 - \cos \theta)$ inverted cycloid: base line $y = 2R$	$s = 4R \sin(\theta/2)$ $s = 2\sqrt{2Ry}$	$\frac{\pi^2 R}{T^2} y + \frac{L^2}{2(I+x_0^2)}$  $-\frac{L^2}{2\left(I + \left\{ R \cos^{-1}\left(\frac{R-y}{R}\right) + \sqrt{2Ry-y^2+x_0} \right\}^2\right)}$
5	$x = R\theta - R \sin \theta + x_0$ $y = R - R \cos \theta$ cycloid	$s = 4R(1 - \cos(\theta/2))$ $s = 4R\left(1 - \sqrt{1 - \frac{y}{2R}}\right)$	$\frac{\pi^2 R}{T^2} y + \frac{L^2}{2(I+x_0^2)}$  $-\frac{L^2}{2\left(I + \left\{ R \cos^{-1}\left(\frac{R-y}{R}\right) - \sqrt{2Ry-y^2+x_0} \right\}^2\right)}$
6	$x = ay + x_0$	$s = \sqrt{1+a^2}y$	$\frac{\pi^2(1+a^2)}{8T^2} y^2 - \frac{L^2}{2(I+(ay+x_0)^2)} + \frac{L^2}{2(I+x_0^2)}$
7	$x = 2\sqrt{ay^3}/3 + x_0$	$s = \frac{2}{3a} [(1+ay)^{3/2} - 1]$	$\frac{\pi^2}{18a^2 T^2} [(1+ay)^{3/2} - 1]^2$  $-\frac{L^2}{2(I+(2\sqrt{ay^3}/3+x_0)^2)} + \frac{L^2}{2(I+x_0^2)}$
8	$x = ay^2/2 + x_0$	$s = (ay\sqrt{1+a^2y^2} + \ln(ay + \sqrt{1+a^2y^2}))/2a$	$\frac{\pi^2}{32a^2 T^2} (ay\sqrt{1+a^2y^2} + \ln(ay + \sqrt{1+a^2y^2}))^2$  $-\frac{L^2}{2(I+(ay^2/2+x_0)^2)} + \frac{L^2}{2(I+x_0^2)}$
9	$y = a \cosh((x-x_0)/a) - a$ $+x_0$	$s = \sqrt{(y+a)^2 - a^2}$	$\frac{\pi^2}{8T^2} [(y+a)^2 - a^2] + \frac{L^2}{2(I+x_0^2)}$  $-L^2/\left(2\left(I + \left\{ a \cosh^{-1}\left(\frac{y+a}{a}\right) + x_0 \right\}^2\right)\right)$

the wire, shaft and support. We will also assume that  $x_0 = 0$ , so that the wire is attached directly to the shaft at the bottom. Starting with (14) we can write

$$V_*(y) = V(y) + \frac{L^2}{2I(1+x(y)^2/I)} - \frac{L^2}{2I}$$

Expanding the second term on the right in powers of  $x(y)^2/I$  we obtain to a first-order approximation

$$V_*(y) = V(y) - \frac{1}{2} \frac{L^2}{T^2} x(y)^2$$

The conservation of angular momentum (12), to a first-order approximation becomes simply  $L = I\omega$  where  $\omega$  is now a constant. Thus the above expression becomes

$$V_*(y) = V(y) - \frac{1}{2} \omega^2 x(y)^2$$

The differential Eq. (15) is now much simpler,

$$1 + x'(y)^2 = \frac{2T^2 \{V'(y) - \omega^2 x(y)x'(y)\}^2}{\pi^2 \left\{V(y) - \frac{1}{2} \omega^2 x(y)^2\right\}}$$

As an example consider the potential of a simple harmonic oscillator  $V(y) = ky^2/2$  and try a straight line solution  $x(y) = ay$ , the differential equation becomes (after simplifying)

$$1 + a^2 = \frac{4T^2}{\pi^2} \{k - a^2 \omega^2\}.$$

Solving for  $a$  we get  $a = \sqrt{4T^2 k - \pi^2/4T^2 \omega^2 + \pi^2}$ . Thus, under a harmonic oscillator potential the tautochrone curve is a straight line with slope  $a$ .

In general the potential for the rotating tautochrone, to a first-order approximation, is

$$V(y) = V_*(y) + \frac{1}{2} \omega^2 x(y)^2 + C.$$

The first term is the potential of a nonrotating tautochrone  $V_*(y)$ , the second term is the potential of a simple harmonic oscillator, and  $C$  is a constant. The second term could be produced by an ideal spring stretched along the  $x$ -axis with one end attached to the bead and at the other to the shaft. As the bead moves down so does the spring. The tension in the spring serves to exactly cancel the centrifugal force  $\omega^2 x$ . Thus, the motion of the bead along the wire, as seen by an observer rotating with the system, will be identical to the motion of the bead of a nonrotating tautochrone of potential  $V_*(y)$ .

## 6 Physical Intuition Behind Tautochrones

There is a simple, beautiful explanation for all tautochrone motion. *All tautochrones act like simple linear springs.* Suppose a mass  $m$  attached to a spring is displaced a distance  $A$  from equilibrium. The time required for the mass to return to the equilibrium position is

$$T = \frac{\pi}{2} \sqrt{\frac{m}{k}} \quad (17)$$

where  $k$  is the spring constant. This time is independent of the displacement  $A$  and thus we have tautochrone motion in every simple spring. The restoring force from the spring is proportional to the distance  $s$  that the spring is stretched:  $F = ks$ . Solving (17) for  $k$  we can write this force as

$$F = \frac{m \pi^2}{4T^2} s. \quad (18)$$

This formula is also valid for any nonrotating tautochrone ([2]).

Let us now examine the forces on the bead (of unit mass) on our rotating tautochrone curve. Starting with relation (2) and replacing the potential by  $V_*(y)$  we get

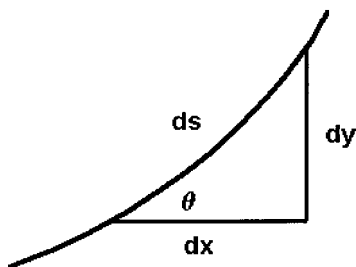


Fig. 2 Geometric meaning of differentials

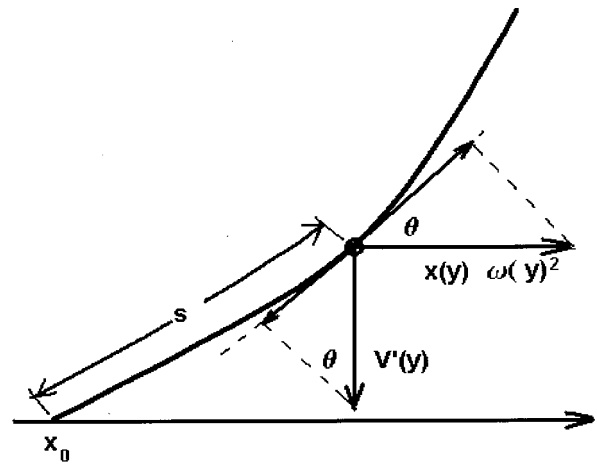


Fig. 3 Why all tautochrones act like simple springs

$$V_*(y) = \frac{\pi^2}{8T^2} s^2.$$

Next use (14) to replace  $V_*(y)$  to obtain

$$V(y) + \frac{1}{2} \frac{L^2}{(I + x(y)^2)} - \frac{L^2}{2(I + x_0^2)} = \frac{\pi^2}{8T^2} s^2.$$

Differentiate with respect to  $y$  and get

$$V'(y) - \frac{L^2 x(y)x'(y)}{(I + x(y)^2)^2} = \frac{\pi^2}{4T^2} s \frac{ds}{dy}.$$

From (12) we see that  $\omega(y)^2 = L^2/(I + x(y)^2)^2$  and thus the above expression can be written as

$$V'(y) - x(y)\omega(y)^2 \frac{dx}{dy} = \frac{\pi^2}{4T^2} s \frac{ds}{dy}.$$

Finally we multiply by  $dy/ds$  to get

$$V'(y) \frac{dy}{ds} - x(y)\omega(y)^2 \frac{dx}{ds} = \frac{\pi^2}{4T^2} s.$$

From Fig. 2 we see that the derivatives in the above expression can be replaced by  $dx/ds = \cos \theta$  and  $dy/ds = \sin \theta$ .

$$V'(y) \sin \theta - x(y)\omega(y)^2 \cos \theta = \frac{\pi^2}{4T^2} s. \quad (19)$$

Using Fig. 3 we see that the term  $V'(y) \sin \theta$  is the component of the force generated by the potential in the direction tangent to the tautochrone curve. We also see that the term  $x(y)\omega(y)^2 \cos \theta$  is the component of centripetal acceleration along the tautochrone curve.

Thus we see that (19) tells us that when the forces acting on our bead are resolved in the direction tangent to the tautochrone curve, then the sum of these forces is proportional to the distance  $s$  from the final point on the tautochrone. This is similar to (18) that describes the simple spring. (Notice that with  $m = 1$  the constants in (18) and (19) are identical.) *The sum of the forces tangent to a tautochrone curve on a moving bead is proportional to the distance measured from the final point to the bead.*

## References

- [1] Flores, E. V., and Osler, T. J., 1999, "The Tautochrone Under Arbitrary Potentials Using Fractional Derivatives," *Am. J. Phys.*, **67**, pp. 718–722.
- [2] McKinley, J. M., 1979, "Brachistochrones, Tautochrones, Evolutes, and Teselations," *Am. J. Phys.*, **47**, No. 1, pp. 81–86.

# Smooth Asymmetric Two-Dimensional Indentation of a Finite Elastic Beam

M. Zhou

Graduate Research Assistant, Civil and Environmental Engineering Department, University of Alabama, Huntsville, AL 35899

W. P. Schonberg

Professor and Chair, Civil Engineering Department, University of Missouri-Rolla, Rolla, MO 65409  
Mem. ASME  
e-mail: wschon@umr.edu

*Standard methods of beam indentation analysis use a beam theory solution to obtain the load-displacement relationship and a Hertz solution to calculate local stresses. However, when the contact length exceeds the thickness of the beam point contact can no longer be assumed and Hertzian relations are no longer valid. This paper presents an improved superposition solution technique that uses a true elasticity solution to obtain the load-displacement relationship in non-Hertzian indentation problems.*  
[DOI: 10.1115/1.1352068]

## Introduction

In this paper, we present an improved solution to the two-dimensional problem of a finite beam of length  $L$  and thickness  $h$  that is loaded *asymmetrically* on its upper surface by a frictionless cylindrical indenter (see Fig. 1). Standard methods of indentation analysis use a beam theory solution to obtain an overall load-displacement relationship and then a Hertzian contact solution to calculate local stresses under the indenter. However, previous modeling efforts have shown that the stress distribution in the region of contact will differ significantly from a Hertzian one when the contact length exceeds the thickness of the beam. In such cases, point contact can no longer be assumed and Hertzian relations are not valid.

Problems of this type were solved previously by Keer and Miller [1] and Peck and Schonberg [2] using a GLOBAL/LOCAL approach that superposed beam theory and elasticity expressions. The technique developed was also applied to cantilever beam indentation by Keer and Schonberg [3,4] and subsequently modified to include beam rotation effects by Zhou and Schonberg [5]. A review of the superposition procedure used by Keer, Schonberg, et al. reveals that it has a problematic aspect: it uses an approximate solution (instead of an elasticity solution) to establish the load-displacement relationship at the contact site.

The improved superposition technique presented in this paper addresses this issue by using a static finite layer solution that is a true elasticity solution. Also, in a manner similar to that used by Zhou and Schonberg [5] to model cantilever beam indentation, the rotation of the beam under the indenter is included in the mixed boundary condition at the contact site. As a result, the final solution takes into consideration all of the prescribed boundary and end conditions and describes more accurately the local surface

deformation due to contact pressure and the global flexural deformation of the beam. The validity of the solutions presented is assessed by comparing the results obtained to the predictions of modified beam theory solutions.

## Generalized Elasticity Solution for a Finite Layer

In this section we present the solution for a finite elastic layer of thickness that is subjected to an arbitrary upper surface pressure distribution. This solution is achieved by the superposition of an elasticity solution for an infinite layer loaded on its upper surface with an elasticity solution for a finite layer subjected to asymmetric bending.

A suitable elasticity solution that represents normal loading on the upper surface of an infinite elastic layer in plane strain with no loading on its lower surface is given by Keer and Miller [1]. To complete the finite elastic layer solution, we introduce the following elasticity solution for the asymmetric bending of a finite layer (thickness  $h$  and length  $L$ ) having end moments  $M_0$  and  $M_1$ :

$$\sigma_{yy} = 0, \quad (1)$$

$$\sigma_{xy} = \frac{V(x)}{2I} y(h-y), \quad (2)$$

$$\sigma_{xx} = \frac{M(x)}{I} \left( y - \frac{h}{2} \right) \quad (3)$$

$$u_x = \frac{1}{D} \left[ b_0 - a_1 y + \frac{2-\nu}{12(1-\nu)} \frac{M_1 - M_0}{L} [2(h-y)^3 - 3h(h-y)^2] + \left[ M_0 x + \frac{M_1 - M_0}{2L} (L_0 + x)^2 \right] \left( y - \frac{h}{2} \right) \right] \quad (4)$$

$$u_y = \frac{1}{D} \left[ a_0 + a_1 x - \frac{1}{2} M_0 x^2 - \frac{M_1 - M_0}{6L} (L_0 + x)^3 \right] - \frac{\nu}{2(1-\nu)D} M(x)(y^2 - hy) \quad (5)$$

$$\bar{\theta}(x) \equiv \frac{1}{h} \int_0^h \frac{\partial u_y}{\partial x} dy = \frac{1}{D} \left[ a_1 - M_0 x - \frac{M_1 - M_0}{2L} (L_0 + x)^2 \right] + \frac{\nu h^2}{12(1-\nu)D} \frac{M_1 - M_0}{L} \quad (6)$$

$$M(x) = M_0 + \frac{M_1 - M_0}{L} (L_0 + x), \quad (7)$$

$$V(x) = \frac{M_1 - M_0}{L} \quad (8)$$

where  $L_0$ ,  $L$ , and  $L_1$  are as shown in Fig. 1,  $D = \mu h^3/6(1-\nu)$ ,  $I = h^3/12$ ,  $M_0$ ,  $M_1$  are end bending moments at  $x = -L_0$  and at  $x = L_1$ , respectively, and  $a_0$ ,  $b_0$ ,  $a_1$  are (as yet) unknown constants. This solution is a superposition of the Airy stress function solutions for asymmetric bending and for pure shear.

Superposing Eqs. (1)–(8) with the corresponding expressions for stresses, displacements, etc., in Keer and Miller [1] yields the generalized elasticity solution for a finite length isotropic elastic layer subjected to an arbitrary upper surface loading. In the next section, we apply appropriate end conditions to this solution to obtain the desired beam indentation problem solutions.

## Asymmetric Beam Indentation Model

The mixed boundary value problems to be solved in this section are those of a simply supported and a fixed-fixed elastic beam that are indented by a cylindrical punch on their upper surface (see again Fig. 1). The solutions of these problems are achieved by application of the mixed boundary conditions at the contact sites

Contributed by the Applied Mechanics Division of THE AMERICAN SOCIETY OF MECHANICAL ENGINEERS for publication in the ASME JOURNAL OF APPLIED MECHANICS. Manuscript received and accepted by the ASME Applied Mechanics Division, May 31, 2000; final revision, Oct. 10, 2000. Associate Editor: M.-J. Pindera.

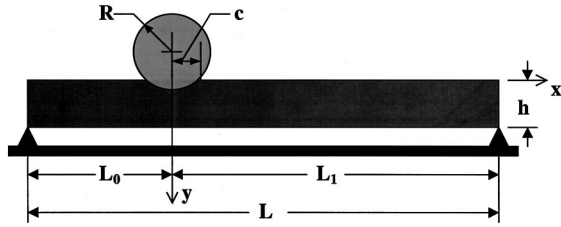


Fig. 1 Indentation of a finite layer

and the appropriate end support conditions in the generalized elasticity solution presented in the preceding section. As in Zhou and Schonberg [5], the boundary condition for both types of beams at contact sites is written as follows:

$$u_y(x,0) = \Delta + \theta_0 x - \frac{x^2}{2R} \quad |x| < c \quad (9)$$

where  $\Delta$  and  $\theta_0$  are the beam upper surface displacement and rotation under the indenter. The two types of end support conditions that need to be satisfied are (1) simple supports (zero moment and displacement at the beam ends), and (2) fixed ends (zero slope and displacement at the fixed ends). By applying these end support conditions to appropriate expressions in the generalized elasticity solution, we obtain a system of four equations for the four unknowns  $a_0$ ,  $a_1$ ,  $M_0$ , and  $M_1$  for each beam type. Once solved, the expressions for these four quantities are used in applying the mixed boundary condition at contact site given by Eq. (9). Following the approach used by Keer, Schonberg, et al. we obtain two coupled Fredholm integral equations of the second kind. These equations have the following forms:

$$\frac{h^3}{6} \psi(x) + \int_0^c \psi(t) K_1(x,t) dt + \int_0^c \phi(t) K_2(x,t) dt + f(x) = -\frac{Dx}{R} \quad (10)$$

$$\frac{h^3}{6} \phi(x) + \int_0^c \phi(t) K_3(x,t) dt + \int_0^c \psi(t) K_4(x,t) dt + g(x) = 0 \quad (11)$$

where the kernels  $K_1$  through  $K_4$  and the functions  $f(x)$ ,  $g(x)$  are given as follows:

#### Simply Supported Ends.

$$K_1(x,t) = - \int_0^\infty \left[ \frac{h^3}{6} \left( \frac{\beta + sh\beta ch\beta}{\beta^2 - sh^2\beta} + 1 \right) \xi x J_0(\xi x) + \frac{x}{2} \frac{\cos(\xi L_0) + \cos(\xi L_1)}{\xi^2} \right] J_0(\xi t) d\xi + \frac{\pi(L_1 - L_0)^2}{4L} x \quad (12)$$

$$K_2(x,t) = \frac{\pi(L_1 - L_0)}{4L} xt \quad (13)$$

$$K_3(x,t) = \frac{h^3}{6} \left( \frac{1}{t} \right) + \frac{h^3}{6} \int_0^\infty \left( \frac{\beta + sh\beta ch\beta}{\beta^2 - sh^2\beta} + 1 \right) \times [J_0(\xi x) - \xi x J_1(\xi x) - 1] J_1(\xi t) d\xi - \frac{3\pi x^2}{8L} t \quad (14)$$

$$K_4(x,t) = -\frac{3\pi x^2}{8L} (L_0 - L_1) \quad (15)$$

$$f(x) = 0, \quad (16)$$

$$g(x) = 0 \quad (17)$$

#### Fixed-Fixed Ends.

$$K_1(x,t) = - \int_0^\infty \left\{ \frac{h^3}{6} \left( \frac{\beta + sh\beta ch\beta}{\beta^2 - sh^2\beta} + 1 \right) \xi x J_0(\xi x) - \frac{h^3}{6L} \frac{x}{\beta - sh\beta} [\sin(\xi L_0) + \sin(\xi L_1)] \right\} J_0(\xi t) d\xi - \frac{3-2\nu}{1-\nu} \frac{\pi h^2}{12L} x \quad (18)$$

$$K_2(x,t) = \frac{h^3}{6L} \int_0^\infty \frac{x}{\beta - sh\beta} [\cos(\xi L_0) - \cos(\xi L_1)] J_1(\xi t) d\xi \quad (19)$$

$$K_3(x,t) = \frac{h^3}{6} \left( \frac{1}{t} \right) + \int_0^\infty \frac{h^3}{6} \left( \frac{\beta + sh\beta ch\beta}{\beta^2 - sh^2\beta} + 1 \right) \times [J_0(\xi x) - \xi x J_1(\xi x) - 1] J_1(\xi t) d\xi \quad (20)$$

$$K_4(x,t) = 0 \quad (21)$$

$$f(x) = \frac{x}{2L} (L_1 - L_0)(M_1 - M_0), \quad (22)$$

$$g(x) = -\frac{3}{4} \frac{x^2}{L} (M_1 - M_0) \quad (23)$$

The functions  $\psi(t)$  and  $\phi(t)$  are related to the symmetric and anti-symmetric components of the surface loading as follows:

$$P = -\pi \int_0^c \psi(t) dt, \quad (24)$$

$$M = -\pi \int_0^c t \phi(t) dt. \quad (25)$$

Once Eqs. (10),(11) are solved to obtain  $\psi(x)$  and  $\phi(x)$ , all necessary quantities can also be readily obtained. The actual solution of Eqs. (10),(11) is performed numerically in nondimensional form. This transformation is obtained using the following nondimensional parameters:  $L_0/h$ ,  $L/h$ ,  $t/c$ ,  $x/c$ ,  $y/h$ ,  $Rh^3\psi(x)/Dc$ , and  $Rh^3\phi(x)/Dc$ , and  $R\Delta/h^2$ . To assess the validity of the elasticity solutions, their predictions for beam displacement are compared with the predictions of beam theory solutions that use as input the contact pressure generated by the elasticity solutions. These solutions are given as follows:

#### Simply Supported Ends.

$$\Delta_{SS} = \frac{L_0 L_1}{3DL} [L_0 L_1 P + (L_1 - L_0) M] + \frac{1}{D} \int_0^c \left( \frac{\pi L_0 L_1}{4L} - \frac{t}{9} \right) t^2 \psi(t) dt + \frac{\pi(L_1 - L_0)}{32DL} \int_0^c t^3 \phi(t) dt \quad (26)$$

#### Fixed-Fixed Ends.

$$\begin{aligned} \Delta_{FF} = & \Delta_{SS} - \frac{L_0^2 L_1^2}{3DL^3} (L^2 - L_0 L_1) P - \frac{L_0 L_1}{6DL^3} (L_1 - L_0) \\ & \times [L^2 + (L_1 - L_0)^2 + L_0 L_1] M \\ & - \frac{\pi L_0 L_1}{12DL^3} [L^2 + 2(L_1 - L_0)^2 + 2L_0 L_1] \int_0^c t^2 \psi(t) dt \\ & + \frac{\pi L_0 L_1 (L_1 - L_0)}{16DL^3} \int_0^c t^3 \phi(t) dt \end{aligned} \quad (27)$$

where  $\Delta_{SS}$  is given by Eq. (26), and  $P$ ,  $M$  are again given by Eqs. (24), (25), respectively.

## Results and Discussion

Solutions to the two types of indentation problems were obtained for  $c/h = 0.25, 0.5, 1.0$  and  $2.0$ ,  $L/h = 10.0$  and  $20.0$ , and for each  $L/h$  value,  $2L_0/L = 1.0, 1.5$ , and  $1.7$  (where  $2L_0/L = 1.0$  corresponds to the case of central indentation studied by Keer and Miller [1]). We note that for  $2L_0/L = 1.7$  and  $L/h = 10$ ,  $c/h = 2.0$  would imply that the contact length would extend past the support; hence,  $c/h = 2.0$  was not considered in this case. For the fixed-fixed beam indentation problem, all calculations are performed with a Poisson's ratio of  $0.3$ . The results of this parametric study were compared with values obtained using the models developed by Keer and Miller [1] and Peck and Schonberg [2] that did not include upper-surface rotation effects.

For small values of  $c/h$  (i.e.,  $c/h \leq 0.5$ ), the predictions of peak contact stress values by the various solutions agreed quite well. However, for  $c/h \geq 1$  the peak stress predictions were found to occasionally differ significantly. This occurred because as  $c/h$  increases, the effects of beam upper surface rotation effects become more pronounced. While the current model incorporates those effects, the previous models do not. Therefore, the various models will match more closely for smaller contact areas and indenter locations that result in minimal rotation effects. For larger contact areas and for indenter locations near beam ends, peak contact stress values predicted by the various models differed by as much as 10–15 percent for both types of beam supports. Finally, we

note that while there were differences in peak contact stress values, the overall shapes of the contact stress distributions were very similar to those presented by Keer and Miller [1] and by Peck and Schonberg [2].

A comparison between the predictions of beam displacement under the indenter generated by the improved solutions developed herein and the predictions of the beam theory solutions showed that the results of the two solutions agreed very well, and that the agreement improved as  $L/h$  increased and  $c/h$  decreased. This can be explained by the following considerations. First, as  $L/h$  increases, the effects of shear deformation on beam response become negligible. Second, as  $c/h$  decreases, the local effects of beam upper surface rotation become negligible. In both cases, while the elasticity solution incorporates those effects, the beam theory solutions do not. Therefore, the two solutions will match more closely for indenter locations that result in minimal shear deformations and for smaller  $c/h$  values.

Differences between the displacement predictions of the elasticity solution developed herein and the predictions obtained using the GLOBAL/LOCAL models developed previously by Keer and Miller [1] and Peck and Schonberg [2] showed fairly minimal differences for small  $c/h$  values and for most  $2L_0/L$  values (typically less than five percent). This was expected because (1) the governing equations of motion for the solution developed herein and the solutions developed by Keer and Miller [1] and Peck and Schonberg [2] are identical for the case of simply supported ends, and (2) beam upper surface rotation effects on beam response are minimal when for small  $c/h$  values. Furthermore, in the case of fixed-fixed beams, as  $2L_0/L \rightarrow 1$  and  $L/h$  increases, the condition of zero rotation angle at the fixed end supports has less of an effect on the contact zone. Therefore, the effects of second order shearing effects on the average beam rotation  $\bar{\theta}$  for the new model become negligible. While the current model incorporates those effects, the previous models do not. Therefore, the newly developed and previous models will match more closely for smaller contact area and indenter locations that result in minimal rotation and shearing effects.

Figure 2 shows the nondimensional load-displacement curves for  $L/h = 10$  and  $20$  fixed-fixed beams where  $2L_0/L = 1.7$ . The

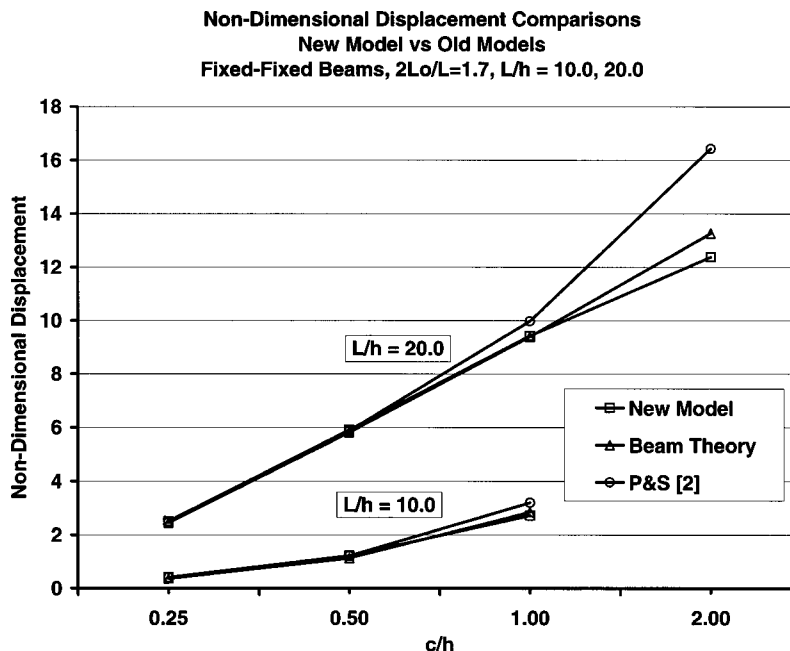


Fig. 2 Nondimensional displacement comparisons, new model versus old models (Keer and Miller [1]; Peck and Schonberg [2]), fixed-fixed beams,  $2L_0/L = 1.7$ ,  $L/h = 10.0$  and  $20.0$

larger differences in some of the indentation scenarios shown in this figure can probably be attributed to limitations in the numerical integrations of the infinite integrals that appeared in the work performed by Peck and Schonberg [2]. According to Peck and Schonberg, it was not possible to integrate the kernels in the fixed-fixed beam equations to the same accuracy as those in the simply supported cases. This was due to the fact that the kernels for simply supported beam equations converged at a rate of  $1/\xi^2$ , while those for the fixed-fixed beams converged at the much slower rate of  $1/\xi$ . In our solution, we have overcome this numerical integration limitation by using exact integration results for expressions involving Bessel functions. This allowed the kernels in the fixed-fixed beam equations to converge at the much faster rate of  $1/sh\xi$ .

Interestingly enough, the value of  $R$  (the radius of the indenter) did not appear to have any bearing on the solution of the governing equations for this problem. That is, the nondimensional stress and displacement values calculated using the model developed herein would appear to be valid for all values of  $R$ ! Mathematically, this occurs because of the nondimensional scheme: in this scheme, all traces of  $R$  are removed by the nondimensionalization process. However,  $R$  *does* have an effect when the nondimensional values of stress and displacement are transformed into real values. While all of the nondimensional predictions of the model may be mathematically possible, they may *not* be physically attainable for some values of  $R$ . For example, the case of  $c/h=2$  is clearly more readily attainable for very large values of  $R$  (as compared to  $h$ ), and significantly less so (if not impossible) for small values of  $R$  (as compared to  $h$ ).

## Summary and Conclusions

The static and dynamic indentation of beams and plates continues to be an intriguing problem, especially for scenarios in which large area contact can be expected to occur. The solution scheme presented herein is a refinement of the approach originally developed for the relatively simple problem of central beam indentation. We found that the results provided by this refinement are, in most cases, not significantly different from those that can be obtained using existing GLOBAL/LOCAL analysis techniques. However, the changes introduced into the modeling process should allow this refined solution technique to more accurately predict internal stress fields due to upper surface indentations. This capability is critical in the case of composite beams or plates where internal damage can appear prior to any evidence of damage on the external beam or plate surface.

## References

- [1] Keer, L. M., and Miller, G. R., 1983, "Smooth Indentation of a Finite Layer," *J. Eng. Mech.*, **109**, pp. 706–717.
- [2] Peck, J. A., and Schonberg, W. P., 1993, "Asymmetric Indentation of a Finite Elastically Supported Beam," *J. Appl. Mech.*, **60**, pp. 1039–1045.
- [3] Keer, L. M., and Schonberg, W. P., 1986, "Smooth Indentation of an Isotropic Cantilever Beam," *Int. J. Solids Struct.*, **22**, pp. 87–106.
- [4] Keer, L. M., and Schonberg, W. P., 1986, "Smooth Indentation of a Transversely Isotropic Cantilever Beam," *Int. J. Solids Struct.*, **22**, pp. 1033–1053.
- [5] Zhou, M., and Schonberg, W. P., 1995, "Rotation Effects in the Global/Local Analysis of Cantilever Beam Contact Problems," *Acta Mech.*, **108**, pp. 49–62.